To The University of Wyoming:

The members of the Committee approve the thesis of Shiqi Zhang presented on November 29, 2011.

Sukky Jun, Chairman (posthumous)

Ray. Fertig

Carl. Frick

Gi-Hyeon Park

APPROVED:

Paul A. Dellenback, Head, Department of Mechanical Engineering

Robert Ettema, Dean, College of Engineering and Applied Science

Zhang, Shiqi, The Effect of Strain on Electronic Structures of Hybrid Graphene-Boron Nitride Monolayer Superlattices, M.S., Department of Mechanical Engineering, May, 2012

Since the discovery of graphene monolayers, a variety of 2D crystals have been explored both theoretically and experimentally. Most recently, domain-hybridized graphene and boron nitride (C-BN) monolayers have successfully been fabricated. Our research group has proposed a 2D superlattice monolayer consisting of well-aligned alternating graphene and boron nitride stripes and shown that this hetero-phase 2D crystalline monolayer is structurally very stable and electronically semiconducting. In this research, we further investigate the feasibility of tailoring the electronic property of C-BN monolayer superlattice by applying mechanical strain. Using the first-principles calculation based on density functional theory, we compute detailed electronic band structures of C-BN superlattices subject to mechanical strain, with respect to stripe width. The dramatic bandgap changes of armchair superlattices are presented and the mechanically tuned spin-polarized metallic properties of zigzag superlattices are demonstrated.

THE EFFECT OF STRAIN ON ELECTRONIC STRUCTURES OF HYBRID GRAPHENE-BORON NITRIDE MONOLAYER SUPERLATTICES

by
Shiqi Zhang

A thesis submitted to Department of Mechanical Engineering
and The Graduate School of University of Wyoming
in partial fulfillment of the requirements
for the degree of

MASTER OF SCIENCE
IN
MECHANICAL ENGINEERING

Laramie, Wyoming
May 2012

ProQuest LLC.
789 East Eisenhower Parkway
P.O. Box 1346
Ann Arbor, MI 48106 - 1346

Dedication

For my families, advisor Sukky Jun, my committee member Carl Frick, Ray Fertig, and Gi-Hyeon Park, my girlfriend Ge Zhu, my friends Fanchao Meng and Xiaobao Li for filling this dreamer's sails.

Acknowledgements

I appreciate the great guide from my academic adviser Professor Sukky Jun. Dr. Jun has patiently and kindly introduced me to the computational material science area by teaching me advanced material science and first- principles calculation. During my M.S. study here, Dr. Jun has taught me how to think and how to get creative ideas for my research. Dr. Jun also gave me a lot of help for my life in the University of Wyoming. I would like to appreciate helpful discussions with Professor Cristian V. Ciobanu from Colorado School of Mines. I would sincerely thank Professor Frick and Professor Fertig from Mechanical Engineering Department and Professor Park from Civil and Architectural Engineering Department for being my committee members and reviewing my thesis. All faculty members in Mechanical Engineering Department would be appreciated for having taught me. Here, I would also thank my parents for supporting me to study in the University of Wyoming. Support from National Science Foundation is gratefully acknowledged.

Shiqi Zhang

The University of Wyoming

May 2012

Contents

Dedication ii

Acknowledgements iii

List of Figures v

List of Tables vii

Chapter 1 Introduction 1

1.1 Motivation 1

1.2 Literature Review 5

1.3 Research Goal 7

Chapter 2 Computational Methods 9

2.1 First-Principles Calculations 9

Chapter 3 Calculation Details 13

3.1 Determination of Bond Length 13

3.2 Superlattice Models 15

3.3 Applying Mechanical Strain 20

3.4 Large Deformation Poisson Effect 22

Chapter 4 Numerical Results and Discussions 31

4.1 Armchair C-BNSL Models subject to Strain 31

4.2 Zigzag C-BNSL Models subject to Strain 36

4.3 Boundary Energy and Boundary Stress 40

Chapter 5 Conclusion 42

References 44

List of Figures

1.1 Superlattice model of GaAs and AlAs on GaAs substrate. 3

1.2 Graphene boron nitride superlattice (C-BNSL) monolayer. 5

3.1(a) Primitive unit cells for individual graphene monolayer 13

3.1(b) Primitive unit cells for individual boron nitride monolayer 13

3.2(a) Total energy curve of graphene primitive unit cells with respect to bond lengths. 14

3.2(b) Total energy curve of boron nitride primitive unit cells with respect to bond lengths. 14

3.3(a) Conventional unit cell of graphene monolayer 15

3.3(b) Conventional unit cell of boron nitride monolayer 15

3.4(a) Example of simulation box: armchair C-BNSL24 16

3.4(b) Example of simulation box: zigzag C-BNSL06. 16

3.5(a) Armchair edge of boron nitride monolayer 17

3.5(b) Zigzag edge of graphene monolayer 17

3.6(a) Armchair C-BN boundary. 17

3.6(b) Zigzag C-BN boundary. 17

3.7 10% normal strain on the x-direction. 21

3.8 Large deformation Poisson Effect in 2D 22

3.9(a) Parallel direction of strain on aC-BNSL model. 23

3.9(b) Perpendicular direction of strain on aC-BNSL model. 23

3.9(c) Perpendicular direction of strain on zC-BNSL model. 23

3.10 Applying the fixed strain of the specific direction on the example model. 24

3.11 Changing the other direction due to large deformation Poisson effect. 25

3.12 Energy curve for 5 % parallel strain on aC-BNSL24 model via incremental strain ... 26

3.13 Poisson Ratios for parallel strain for aC-BNSL24.. 27

3.14 Poisson Ratios for perpendicular strain for aC-BNSL24. 27

3.15 Poisson ratios for different models and different direction of strain. 28

4.1 Energy gap curve for aC-BNSL24 with parallel strain. 32

4.2 3D plot of energy gap of aC-BNSL with parallel strain 32

4.3 Energy gap curve for aC-BNSL24 with perpendicular strain. 33

4.4 3D plot of energy gap of aC-BNSL with perpendicular strain. 33

4.5(a) Contour plot of aC-BNSL with parallel. 34

4.5(b) Contour plot of aC-BNSL perpendicular strain 34

4.6(a) Lateral view plot of aC-BNSL with parallel strain 35

4.6(b) Lateral view plot of aC-BNSL with perpendicular strain 35

4.7 Electronic Band structure for different zC-BNSL models without strain. 37

4.8 Spin polarized zC-BNSL energy gaps without strain. 38

4.9 The direction of perpendicular strain on zC-BNSL10. 38

4.10 Electronic band structures of zC-BNSL10 with increasing perpendicular strain. 39

4.11 Electronic band structures of zC-BNSL20 with increasing perpendicular strain. 40

4.12(a) Changing pattern of spin-up band of zC-BNSL subject to perpendicular strain. .. 41

4.12(b) Changing pattern of spin-down band of zC-BNSL subject to perpendicular strain. 41

List of Tables

Table 3.1 Total energy of three methods to build C-BNSL models. 19

Table 3.2 Poisson ratios with respect to 15 % parallel strain on different aC-BNSL models. 28

Table 3.3 Poisson ratios with respect to 15 % perpendicular strain on different aC-BNSL models. 29

Table 3.4 Poisson ratios with respect to 10 % perpendicular strain on different zC-BNSL models. 29

Chapter 1

Introduction

1.1 Motivation

Carbon is a primary material for life and the basis of all organic chemistry. Due to the flexibility of its bonding, carbon-based systems show an unlimited number of structures in nanomaterials, such as graphite, which can be viewed as a stack of graphene layers; carbon nanotubes, which is rolled-up cylinders of graphene; and fullerenes (C_{60}), which are molecules consisting of wrapped graphene by the introduction of pentagon on the hexagonal lattice. Among systems with only carbon atoms, graphene plays an important role since it is the basis for the understanding of the electronic properties in other allotropes.

Graphene is an allotrope of carbon, whose structure is one-atom-thick planar sheets of sp^2-bonded carbon atoms that are densely packed in a honeycomb crystal lattice [1]. Since its successful fabrication in 2004 [2], graphene has attracted tremendous interest from researchers to explore its properties both theoretically and experimentally. They found that graphene has some unique properties. Intrinsic graphene is a semi-metal or zero-gap semiconductor and has a breaking strength 200 times greater than steel, which means graphene appears to be one of the strongest materials ever tested [3].

Graphene is a promising candidate for making a smaller and faster transistor because its electron mobility is an order of magnitude higher than that of silicon. However, the lack of an obvious band gap from graphene is a formidable problem, resulting in difficulties controlling the carrier type. Therefore, several strategies have been investigated to open a clear band gap in graphene,

such as applying mechanical strain, creating a potential difference in bilayer graphene, and patterned hydrogenation.

After the discovery of graphene, researchers began to think that two-dimensional (2D) nanomaterials were more attractive for use in next-generation electronic nano-devices because compared to one-dimensional nanomaterials, 2D nanomaterials are relatively easy to fabricate complex structures. Therefore researchers and scientists started to focus on fabricating and investigating 2D nanomaterials which have the hexagonal lattices similar to graphene. Over past several years, a variety of crystal hexagonal nanomaterials in 2D have been fabricated and explored, such as boron nitride (BN) monolayer. Free standing single layer BN was successfully fabricated in 2009 [4]. Researchers synthesized BN monolayer via controlling energetic electron beam irradiation through a sputter process [5]. The boron-nitrogen bond length is 0.143 nanometers [4], which is similar to the carbon-carbon bond length of graphene. The carbon-carbon bond length of graphene is 0.142 nanometers [6]. Different from a graphene sheet, a zero-gap semimetal, BN sheet display insulating characteristics due to the large ionicity of boron and nitrogen atoms [7].

The reason why successful fabrication of BN monolayer is attractive to our research is as follows. After the discovery of graphene, researchers tried to design an interface between graphene and other honeycomb crystalline nanomaterial in order to tailor the electronic properties of this graphene-based material. But the large difference of bond lengths, makes it unfeasible to build. For example if the interface is between a silicon-carbide (SiC) monolayer and graphene, since the silicon-carbon bond length in SiC monolayer is 0.178 nanometers which is much bigger than carbon-carbon bond length in graphene, thus stretching graphene or compressing SiC monolayer

have to exist for fabricating the interface. This stretching or compressing process will distort or even break the hexagonal lattice in graphene or SiC monolayer. Due to the similarity of bond length between graphene and BN monolayer, interface of these two materials will keep the hexagonal lattice for both of them. Difference of electronic properties between graphene, semiconductor, and BN monolayer, insulator, is also an important reason to fabricate the hybrid structure consisting of graphene and BN monolayer.

Most recently, Ci *et al.* [8] successfully fabricated domain-hybridized graphene and BN (C-BN) monolayer. Our research group proposed to design a nanomaterial based on graphene and BN monolayer. The nanomaterial is constructed on the heterostructure of superlattice model. Superlattice model is a concept in three-dimensions (3D). It describes a periodic structure of layers of two or more materials. Fig. 1.1 illustrates a gallium arsenide (GaAs) and aluminum arsenide (AlAs) superlattice on the substrate of GaAs.

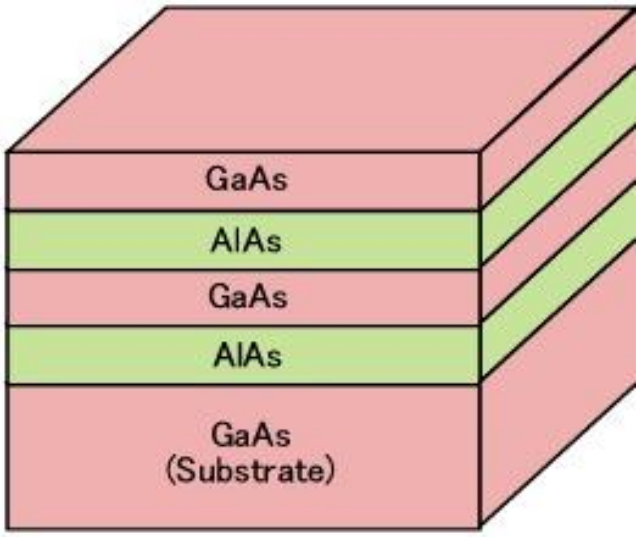

Fig. 1.1 Superlattice model of GaAs and AlAs on GaAs substrate.

This 3D superlattice model has been developed into a 2D concept. Our research group proposed to form a 2D superlattice atomic film which is consisting of the graphene and hexagonal boron nitride monolayer. The graphene-boron nitride superlattice (C-BNSL) monolayer consists of well-aligned and alternating graphene stripes and boron nitride stripes as shown in Fig. 1.2. The C-BNSL includes graphene-boron nitride (C-BN) interface section, which we term the C-BN boundary.

Ci revealed that hybridized BN and graphene domain shows structural features and a band gap that have not been found in graphene, hexagonal BN monolayer or boron- and nitrogen-codoped graphene [8]. Therefore C-BN boundary in C-BNSL should play a key role for tuning the electronic properties.

In this study the effect of mechanical strain on band gap was examed. The maximum in-plane mechanical strain exerted on C-BNSL monolayer was 20 %. This research also details how to incorporate Poisson effect when applying mechanical strain on C-BNSL monolayer.

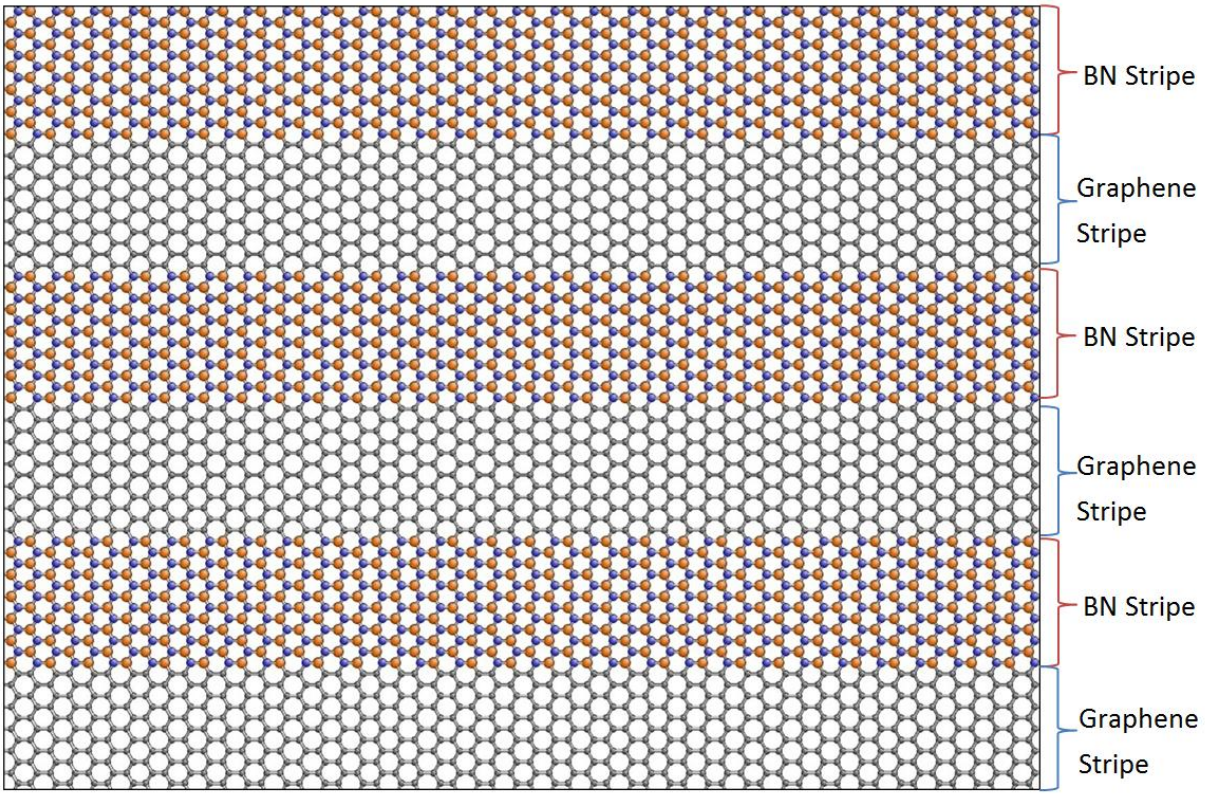

Fig. 1.2 Graphene boron nitride superlattice (C-BNSL) monolayer.

1.2 Literature Review

Many studies have been performed to investigate the effect of mechanical strain on graphene-based materials. Researcher explored the effect of strain on phonon instability [9] and optical conductivity [10] of graphene. Scientists investigated the strain effect on changing of electronic properties of carbon nanotube [11-15]. Studies of graphene on top of SiO_2 [16] or SiC surface [17] revealed a moderate strain induced by surface corrugations or lattice mismatch. Among these researches, the interplay between electronic property of graphene and mechanical strain is one of the most important areas. Several remarkable discoveries of electronic properties of graphene have been found. With symmetrical strain distribution, graphene is always a zero band-

gap semimetal. However, asymmetrical strain distribution on graphene gives an open band gaps [18]. This result indicates that the nature of band structure of graphene monolayer has strong relation to its lattice symmetry. Graphene also remains semimetallic under small strain on arbitrary directions [19]. If the magnitude of strain is less than 26.2 %, no energy gap opens with the zigzag strain (strain along the zigzag chain direction). Graphene with the armchair strain (strain along the armchair chain direction) also has no energy gap up to strain magnitude of 30 % [20].

As mentioned above, several methods exist to open an obvious band gap of graphene. First is the effect of shear and multiaxial strain [21, 22]. Second is to open a gap in bilayer graphene under response to an external electric field [23]. Third is tuning the band gap of graphene by modifying the coverage of atomic hydrogen on graphene [24-28]. In addition to these three strategies, the most promising solution could be cutting graphene down to nanometer-sized graphene nanoribbons [29]. However, the mechanism of unzipping the carbon nanotubes or graphene directly from the edge in to graphene nanoribbons remains unclear [30-33]. In-depth understanding of the underlying electronic functionality is needed.

In contrast to semimetallic graphene, BN monolayer is an insulator due to the large gap between conduction and valence bands. Heterostructures based on graphene and boron nitride monolayer have attracted tremendous attention from researchers and scientists, such as a patch of graphene embedded in hexagonal boron nitride monolayer [34], or atoms of different element doping into the graphene monolayer [35]. Li *et al.* [34] investigated the electronic properties of graphene quantum dots embedded in a hexagonal boron nitride sheet, and they found that the orbital

hybridization between 2*p* orbitals of B, N and C and the quantum confinement together determine the energy gaps of quantum dots.

Other nanomaterials based on graphene and hexagonal boron nitride have also been studied, such as nanoribbons and nanotubes. Boron nitride nanoribbons have large band gaps [36] similar as BN monolayer. Comparing with the band gaps of graphene nanoribbons, which changes with respect to their width, the band gaps of boron nitride nanoribbons do not change significantly with width [37]. Because of this notable difference, and also there exists a similarity of bond length between graphene and boron nitride monolayer as mentioned above, therefore the heterostructure of graphene and BN attracts great attention. Some experimental work has been done on boron-doped graphene nanotubes [38, 39] and nitrogen-doped graphene nanotubes [40, 41]. Du *et al.* [42] found that carbon atom substitution for either single boron or a single nitrogen atom in boron nitride nanoribbons could induce spontaneous magnetization, which is independent of the site of substitution or the type of boron nitride nanoribbons.

1.3 Research Goal

Motivated by the experimental and theoretical work mentioned above and due to the successful fabrication of domain hybrid graphene and boron nitride monolayer, this research is focused on the graphene boron nitride superlattice (C-BNSL) monolayer. This study is to investigate the feasibility of tailoring the electronic property of the C-BN superlattice monolayer by applying mechanical strain and considering large deformation Poisson effect. Using the first-principles calculation which is based on the density functional theory, we compute the detailed electronic band structures of C-BN

superlattices monolayer subject to in-plain strain with respect to the stripe width. Our group proposed to tune the electronic properties of C-BN superlattice monolayer by applying mechanical strain.

Chapter 2

Computational Methods

2.1 First-principles Calculations

First-principles calculation (or *ab initio*, a Latin term meaning "from the beginning") is a method used to solve Schrödinger's equation without making any empirical model or introducing any experimental or empirical parameters. Because this method starts from well-established fundamental physical laws, it has relatively high accuracy. The time independent, nonrelativistic Schrödinger's equation is written as

$$H\Psi = E\Psi \tag{2.1}$$

where H is the Hamiltonian operator, and Ψ is a set of solutions or eigenstates of Hamiltonian. Associated with each eigenstate, there is an eigenvalue E, a real number that can satisfy the eigenvalue equation. The detailed definition of the Hamiltonian depends on the specific physical system. For instance, when systems have multiple electrons and multiple nuclei, Schrödinger's equation has the form

$$\left[-\frac{\hbar^2}{2m}\sum_{i=1}^{N}\nabla_i^2 + \sum_{i=1}^{N}V(\vec{r_i}) + \sum_{i=1}^{N}\sum_{j<i}U(\vec{r_i},\vec{r_j})\right]\Psi = E\Psi \tag{2.2}$$

where m is the mass of the electron, and E is the ground state energy of electrons. In Eq. (2.2), the three terms in the bracket are: the kinetic energy of electron, the interaction energy between each electron and the collections of atomic nuclei, and the interaction between different electrons in order. Ψ is the electronic wave function of spatial coordinates of N electrons given as

$$\Psi=\Psi(\vec{r_1},...,\vec{r_N}) \tag{2.3}$$

By solving the above Schrödinger's equation (Eq. 2.2), the ground state energy can be obtained for the system. However, there are some problems when solving for a large number of electrons. There are three dimensions for each electron, thus all together 3*N* dimensions exist. For example, if one system has 100 Pd atoms (46 electrons for each Pd atom), then there are more than 10,000 dimensions. It could be very time intensive to compute since this system has so many dimensions. Another problem is that it is impossible to directly observe the wave function for any particular set of coordinates. The quantity one can measure is the probability when *N* electrons are at a particular set of coordinates, $\vec{r_1}$,…, $\vec{r_N}$. This probability can be expressed as $\Psi^*(\vec{r_1},...,\vec{r_N})\Psi(\vec{r_1},...,\vec{r_N})$, where the asterisk denotes a complex conjugate**.** Thus, density-functional theory comes to people's mind, which is based on two fundamental mathematical theorems proved by Kohn, Hohenberg and Sham in two publications in 1960s [43, 44]. Hohenberg and Kohn have proven two theorems [43], first of which states that "the ground-state energy from Schrödinger's equation is a unique functional of electron density." The electronic density at a particular position in space, $n(\vec{r})$, is given as

$$n(\vec{r}) = 2\sum_i \Psi_i^*(\vec{r})\Psi_i(\vec{r}). \tag{2.4}$$

The summation term in Eq. (2.3) is the probability that an electron in an individual wave function is located at the position $\vec{r}$. The second Hohenberg and Kohn theorem [44] states that "the electron density that minimizes the energy of the overall functional is the true electron density corresponding to the full solution of the Schrödinger's equation." Therefore, if the "true"

functional form is known, then finding the minimized functional by varying electron density is straightforward.

The energy functional is given as

$$E[\{\Psi_i\}] = E_{known}[\{\Psi_i\}] + E_{XC}[\{\Psi_i\}] \tag{2.5}$$

where $E_{XC}[\{\Psi_i\}]$ is the exchange-correlation functional and it is defined to include all the quantum mechanical effects that are not included in the "known" terms. E_{known} has the form

$$E_{known}[\{\Psi_i\}] = -\frac{\hbar^2}{m}\sum_i \int \Psi_i^* \nabla^2 \Psi_i d^3r + \int V(\vec{r}) n(\vec{r}) d^3r + \frac{e^2}{2}\iint \frac{n(\vec{r}) n(\vec{r'})}{|\vec{r} - \vec{r'}|} d^3r d^3r' + E_{ion}. \tag{2.6}$$

The terms on the right-hand side are, in order, the electron kinetic energies, the Coulomb interactions between the electrons and the nuclei, the Coulomb interactions between pairs of electrons, and the Coulomb interactions between pairs of nuclei [45].

Kohn and Sham have shown that finding the right electron density can be expressed in a way that involves only a single electron [46]. The Kohn-Sham equation has been given as

$$\left[-\frac{\hbar^2}{2m}\nabla^2 + V(\vec{r}) + V_H(\vec{r}) + V_{XC}(\vec{r})\right]\Psi_i(\vec{r}) = \varepsilon_i \Psi_i(\vec{r}). \tag{2.7}$$

Comparing with Eq. (2.2), there is no summation here because one can only get single-electron wave functions $\Psi_i(\vec{r})$ depending on three spatial variables. On the left-hand side, V, V_H, and V_{XC} are three potentials. In order to solve these Kohn-Sham equations, an initial and trial electron density have to be defined, and then the single-particle wave function Ψ can be found.

By substituting this single-particle wave function into Eq. (2.3), the new electron density could be obtained. Then the Kohn-Sham equation can be solved again by using the calculated electron density. Iteratively as the previous steps until the calculated electron density is identical as the one used to solve the Kohn-Sham equations, then the total energy can be obtained by using this calculated electron density which has been defined as ground-state electron density [45].

In this study, DFT total-energy calculations were performed by employing a computer program named Spanish Initiative for Electronic Simulation with Thousands of Atoms (SIESTA) [47]. It uses the standard Kohn-Sham self-consistent density-functional method in the local density approximation (LDA) or generalized gradient approximation (GGA). The SIESTA program, computes several quantities such as total and partial energies, atomic forces, stress tensor, electric dipole moment, electric density, and band structure. Due to these various functions, SIESTA has popularly been employed in various research fields such as material science, computational chemistry, and theoretic physics.

Chapter 3

Calculation Details

3.1 Determination of Bond Length

Lattice constant refers to the constant distance between unit cells in a crystal lattice. Lattices in three dimensions generally have three lattice constants. However, in this study, only two lattice constants of the conventional unit cells need to be determined, since both graphene and boron nitride monolayer crystals have a low dimensional, 2D, hexagonal crystal structure. The bond length, 1.424 Å for graphene [6] and 1.438 Å boron nitride [4] monolayer, has been chosen in order to find the lattice constants according to the reference.

To find the lattice constant, two-atom primitive unit cells for graphene and boron nitride monolayer were needed and they are marked as red rhombus in Fig. 3.1. The primitive unit cell is a minimum-area cell that can fill all space with translational symmetry. To get the lattice constants for individual graphene and boron nitride monolayer, we need to find the carbon-carbon and boron-nitrogen bond length first.

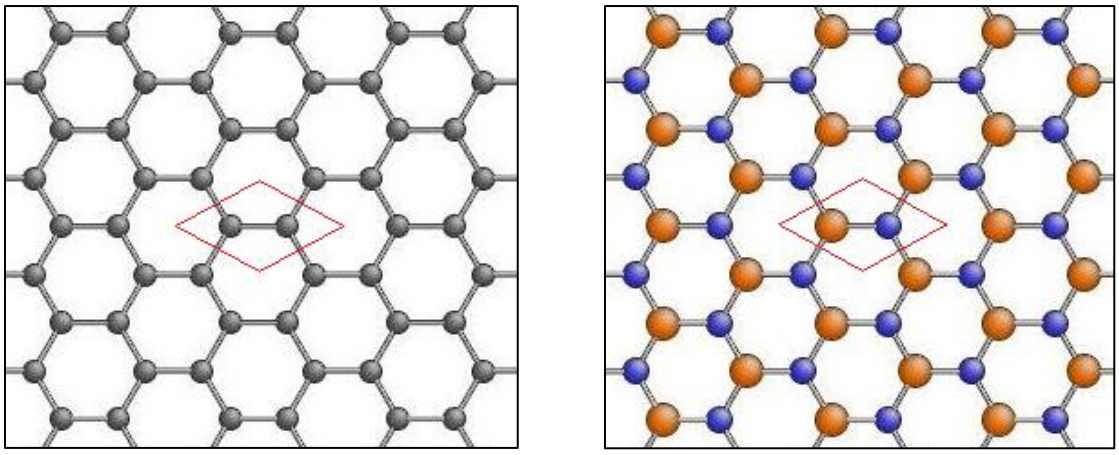

(a) (b)

Fig. 3.1. Primitive unit cells for individual graphene (a) and boron nitride (b) monolayer.

The following steps were used to find the bond length for graphene monolayer. Firstly, a range of bond lengths for graphene monolayer can be set according to the reference [48], from 1.418 Å to 1.427 Å. Values, which are slightly around 1.424 Å as the reference, were picked in this range as bond lengths. Then we used these chosen values to create several primitive unit cells. Next the total energy each primitive unit cell contains was calculated under a fully periodic boundary condition by the first-principles calculations. Then collecting the data of total energy, we can get a smooth curve of total energy with respect to bond lengths. The smooth curve for graphene monolayer of total energy is shown as Fig. 3.2 (a). In this curve, there has a primitive unit cell whose total energy is smaller than the other primitive unit cells. The value to build this primitive unit cell is the carbon-carbon bond length of graphene monolayer. The same procedure is applied to find the boron-nitrogen bond length for boron nitride monolayer. The values we found are 1.422 Å for carbon-carbon bond length of graphene monolayer and 1.438 Å for boron-nitrogen bond length of boron nitride monolayer.

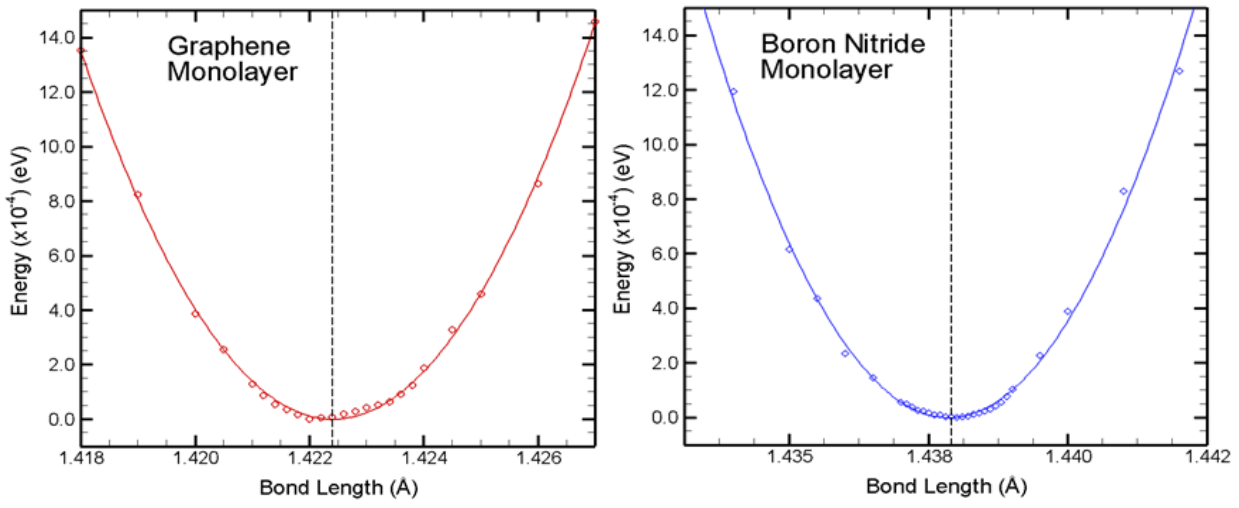

(a) (b)

Fig. 3.2. Total energy curve of graphene (a) and boron nitride (b) primitive unit cells with respect to bond lengths. Dash line is the guide indicating the corresponding bond length.

In order to completely relax the primitive unit cell with bond length of 1.422 Å for graphene and 1.438 Å for boron nitride monolayer, it need to be optimized again by the conjugate gradient optimization. And the cell size is allowed to change, so we can check if atoms change their positions. To further verify that this bond length is the most optimized one, a 4-atom unit cell, conventional unit cell as highlighted rectangular in Fig. 3.3, was generated and optimized with same criteria as before. After optimization, it is noticed the atoms do not change their positions. Therefore, 1.422 Å and 1.438 Å were used as the bond length of graphene and boron nitride monolayer crystal. Due to the geometry relation between the bond length and the lattice constant of conventional unit cell, the lattice constant of conventional unit cell for graphene and boron nitride monolayer can be found respectively from the above bond length for individual graphene and boron nitride monolayer.

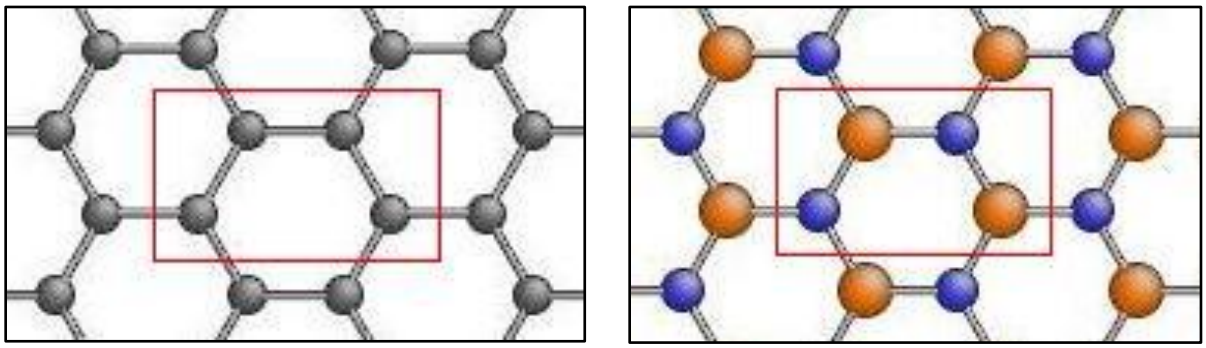

(a) (b)

Fig. 3.3 Conventional unit cell of graphene monolayer (a) and boron nitride monolayer (b).

3.2 Superlattice Models

Before the computation of the energy gap for graphene boron nitride superlattice (C-BNSL) monolayer, superlattice models were generated with different widths based on the 4-atom

conventional unit cell. In order to compute the total energy gap, C-BNSL supercell is placed in a fully periodic three-dimensional (3-D) orthogonal simulation box (Fig. 3.4). 15 Å vacuum spaces are introduced in the z-direction which is perpendicular to the C-BNSL monolayer in order to remove spurious interactions between periodic monolayers.

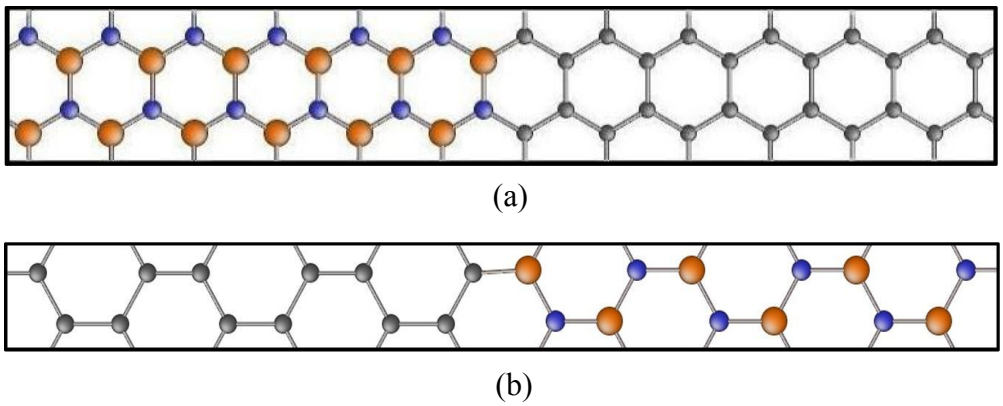

(a)

(b)

Fig. 3.4 Example of simulation box for armchair C-BNSL24 (a) and zigzag C-BNSL06 (b)

The method to name the boundary edge of graphene and boron nitride monolayer follows the conventional naming method. The edge is named as armchair edge if the atoms at the edge are arranged as atoms near the arrow line in Fig. 3.5 (a). The zigzag edge consists of atoms at the edge which are arranged as atoms near the arrow line in Fig. 3.5 (b). To form the graphene boron nitride superlattice monolayer, the C-BN boundary must exist. From Fig. 1.2, the C-BN boundary matches graphene stripes and BN stripes. The C-BN boundary matches same grahpene edge and boron nitride edge. There are two types of boundary: armchair and zigzag C-BN boundary. An armchair C-BN boundary is illustrated in Fig. 3.6 (a). The armchair boundary of the C-BN superlattice model is matched by two armchair edges from both graphene monolayer and boron nitride monolayer. Similarly, the zigzag boundary is matched by two zigzag edges of graphene monolayer and boron nitride monolayers. The blue rectangular in Fig. 3.6 (b) is indicated the zigzag C-BN boundary.

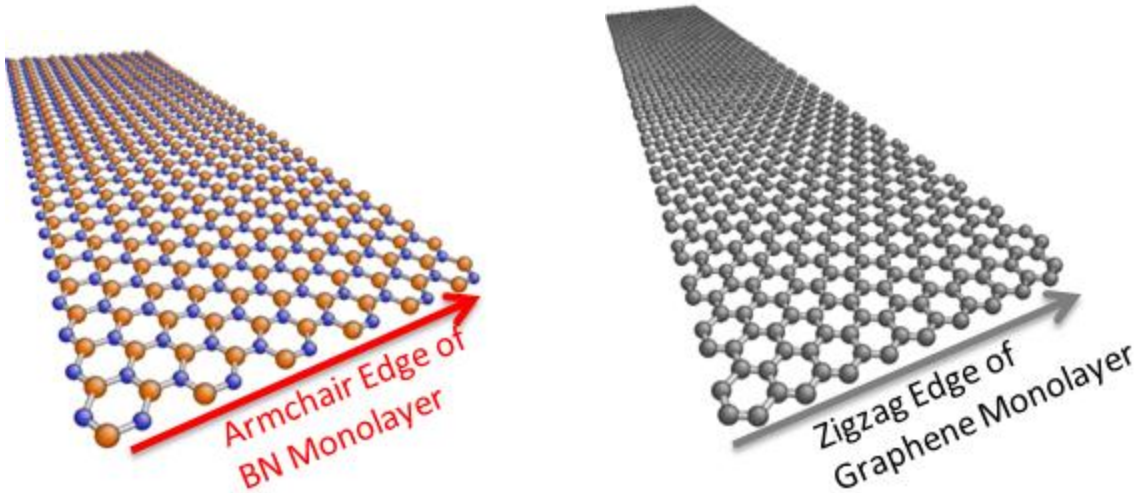

(a) (b)

Fig. 3.5 Armchair edge of boron nitride monolayer (a) and zigzag edge of graphene monolayer (b).

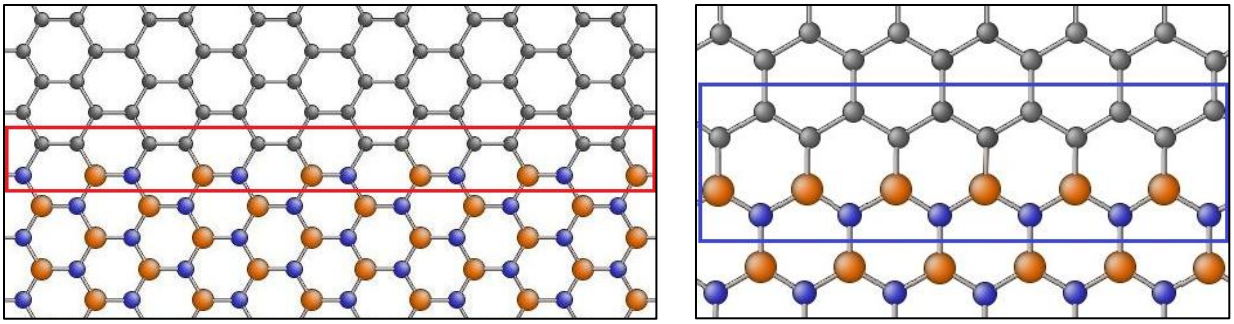

(a) (b)

Fig. 3.6 Armchair C-BN boundary (a) and zigzag C-BN boundary (b).

The superlattice models follow the conventional naming method. For example, graphene boron nitride superlattice monolayers which contain armchair C-BN boundary are called as aC-BNSLn, where n is the number of chains in the width direction. Similarly, graphene boron nitride superlattice monolayer whose C-BN boundary type is zigzag are called as zC-BNSLn, where n is the number of chains in the width direction. Examples as aC-BNSL24 and zC-BNSL06 (Fig.3.4) have been selected to illustrate the naming method of C-BNSL models.

In this study, totally 19 aC-BNSL models and 7 zC-BNSL models were built, which cover width range from 14.60 Å to 59.44 Å for armchair C-BN superlattice models and 21.57 Å to 47.45 Å for zigzag C-BN superlattice models. The energy cutoff and energy shift parameters are set as 250 Ry and 0.01 Ry respectively for energy gap calculations of armchair models. For zigzag models, these parameters are set as 200 Ry of energy cutoff and 0.01 Ry of energy shift.

To calculate the energy gap of each armchair C-BN superlattice model, the *k*-point mesh is selected in the way that 16×m×1 where m is kept as an integer resulting from 16 divided by the number of 4-atom conventional unit cell in the width direction. For example, 16×(16/4)×1 *k*-point mesh is chosen for aC-BNSL08, 16×(16/5)×1 *k*-point mesh is chosen for aC-BNSL10, and 16×1×1 is also chosen for the models which have more than sixteen 4-atom conventional unit cells in the width direction. For zigzag C-BN superlattice models, the *k*-point mesh are selected by a similar way, but with the *k*-point of 24. Therefore, *k*-point mesh has been selected as 24×m×1 for zigzag models, where integer m can be obtained from 24 divided by the number of 4-atom conventional unit cell in the width direction. For example, 24×(24/2)×1 *k*-point mesh is for zC-BNSL04, 24×(24/3)×1 *k*-point mesh is for zC-BNSL06, and 24×1×1 *k*-point mesh is for all zC-BNSLs which have more than twenty-four 4-atom conventional unit cells in the width direction has been selected.

Before any C-BNSL models are actually built, it needs a rational way to form the C-BNSL models, since the lattice constant of graphene monolayer is smaller than that of the boron nitride monolayer, which means that we need to make the graphene stripes longer to match the boron nitride stripes or make the boron nitride stripes shorter to match the graphene stripes. Our research group considered three different methods to simulate the C-BNSL models: stretching

the graphene monolayer, compressing the boron nitride monolayer, or a half-stretching the graphene monolayer and half-compressing the boron nitride monolayer. These three different methods are used to build a same C-BNSL model with exact width. After calculating the total energy each model contains by the first-principles calculation, we compared the results. Table 3.1 lists the results of total energy with respect to the three different methods to build C-BNSL models. It indicates that the model of stretching graphene has the lowest total energy. It means that the model of stretching graphene monolayer is a more stable method than the other two ones to build C-BNSL monolayers. Thus all other C-BNSL models will be built by stretching graphene monolayer.

Table 3.1 Total energy of three methods to build C-BNSL models.

Method to Build C-BNSL Models	**Total Energy (eV)**
Compressing BN Monolayer	-4014.89899
Stretching Graphene Monolayer	-4035.37386
Half Stretching – Half Compressing	-4035.37306

After we determined the method to create the C-BNSL models, all the C-BNSL models need to be optimized. Strain will be applied on the C-BNSL models after this optimization. Also we will consider the large deformation Poisson effect on the models after this optimization. To do so, we set the atomic structures, which the graphene sheets have been perfectly stretched and matched with the boron nitride sheet, as the input coordinates and set all the parameters as the ones in energy gap calculations, then apply the first-principles calculation to optimize the atomistic structures. To fully optimize the atomic structure, conjugate gradient (CG) steps need to be set as 300. The calculation of SIESTA program should stop when the results meet the converge value. Based on the size of the C-BNSL models in this research, 300 CG steps is large enough for

convergence to happen. Therefore the relaxed atomic structures from the output file of SIESTA program will be used for next study. Totally there are 19 armchair C-BNSL models and seven zigzag C-BNSL models. Next we will determine how to apply mechanical strain and consider the large deformation Poisson effect on these C-BN superlattice monolayers.

3.3 Applying Mechanical Strain

Strain is a description of deformation in terms of relative displacement of particles in the deformed body. The relative displacement is between a reference configuration (initial configuration) and a current configuration (deformed configuration). Similar to stresses, strain can also be classified as normal strain and shear strain. Normal strain is the strain that acts perpendicular to the face of an element. The strain acts along the face of an element is called as shear strain. In this study, normal strain is the only type of strain which will be applied on all the C-BNSL models.

A variety of strain measurements have been defined in continuum mechanics, such as Cauchy strain, stretch ratios, and logarithmic strain. In this research the Cauchy strain was used. The Cauchy strain (engineering strain) is expressed as the ratio of total deformation to the initial shape of the material body in which the forces are being applied. The equation for engineering strain can be expressed as Eq. (3.1). ΔL is the length change in the direction of forces being applied, L is the original length of the line element, and l is the length of the deformed line element.

$$\varepsilon = \frac{\Delta L}{L} = \frac{l-L}{L} \tag{3.1}$$

After determining the type of the strain we will use in this research, the method of applying strain to the C-BNSL models must be fixed. Fig 3.7 shows how 10 % normal strain in x-direction was applied. In Fig 3.7 solid lines represent the initial configuration, and the dash lines represent the body after stretching. The rectangular of ABCD is the initial body and AEFD is the deformed body. Based on the definition of engineering strain, 10 % normal strain in the x-direction means the length of BE is one-tenth of length of AB, which is shown as Eq. (3.2)

$$\varepsilon = \frac{\Delta L}{L_{AB}} = \frac{L_{BE}}{L_{AB}} = \frac{L_{AE} - L_{AB}}{L_{AB}} \tag{3.2}$$

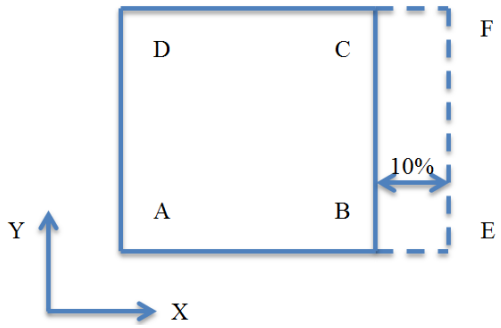

Fig. 3.7 10 % normal strain on x-direction.

Therefore, to apply the mechanical strain on C-BNSL models, a parameter should be multiplied on the atomistic coordinate of C-BNSL models. For example, if 10 % normal strain in x-direction needs to be applied on aC-BNSL10, so 1.1 is the parameter should be multiplied on every X coordinates of aC-BNSL10 and keep all Y coordinates unchanged. After we multiply the specific parameter by the atomistic distance of C-BNSL models that we got after optimazation from Section 3.3, the strain has been applied successfully on all C-BNSL models.

3.4 Large Deformation Poisson Effect

When a material is stretched in one direction, the other two directions perpendicular to the stretching direction tend to contract. This phenomenon is called the Poisson effect. Fig 3.7 illustrates the Poisson effect in 2D. The stretching is in x-direction and the material contracts in y-direction. Poisson ratio is the ratio of the fraction of expansion divided by the fraction of contraction.

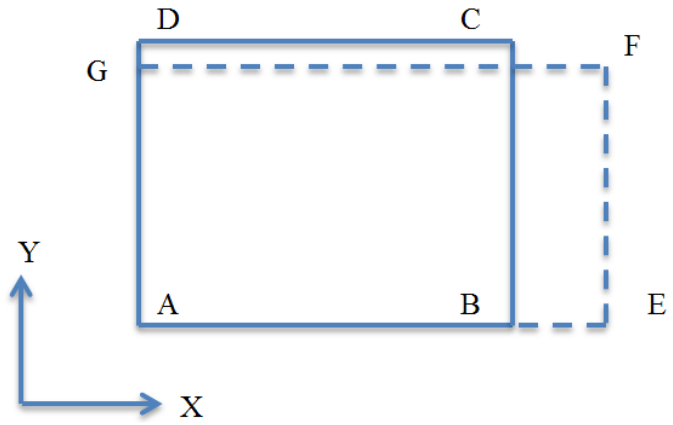

Fig. 3.8 Large deformation Poisson Effect in 2D.

In Fig 3.8, solid lines represent the initial configuration, and the dash lines represent the deformed body. If we neglect the Poisson effect as in section 3.3, the line elements AG and EF will not become shorter. However, the deformation Poisson effect will shrink the AG and EF line elements instead of unchanged.

Assuming that the material is stretched or compressed in an axial direction (x-direction) as strain ϵ_x, and the other two directions (y and z direction) happen to be compressed or stretched as ϵ_y and ϵ_z. The Poisson ratio can be mathematically expressed in Eq. (3.3) as follows. The negative sign in Eq. (3.3) makes Poisson ratio positive.

$$\nu = -\frac{\epsilon_y}{\epsilon_x} = -\frac{\epsilon_z}{\epsilon_x} \tag{3.3}$$

In our research, the direction along the C-BN boundary direction is x-direction. The direction perpendicular to x-direction is y-direction. Three directions of strain were defined on C-BNSL monolayers. They are: x-direction of strain on armchair graphene-boron nitride superlattice (aC-BNSL) monolayers, y-direction of strain on aC-BNSL monolayers and y-direction of strain on zigzag graphene-boron nitride superlattice (zC-BNSL) monolayers. We will consider following ways to name these directions of strain in this research. The strains are denoted by their directions with respect to the C-BN boundary direction. For example, x-direction of strain is called parallel strain and y-direction of strain is called perpendicular strain.

Therefore the Poisson ratios we should find in this study include: (1) Poisson ratios for aC-BNSL models subject to parallel strain, (2) Poisson ratios for aC-BNSL models subject to perpendicular strain, and (3) Poisson ratio for zC-BNSL models subject to perpendicular strain. Fig. 3.9 (a) and (b) illustrates parallel and perpendicular direction of strain on aC-BNSL models. Fig. 3.9 (c) indicates the perpendicular direction of strain on zC-BNSL models.

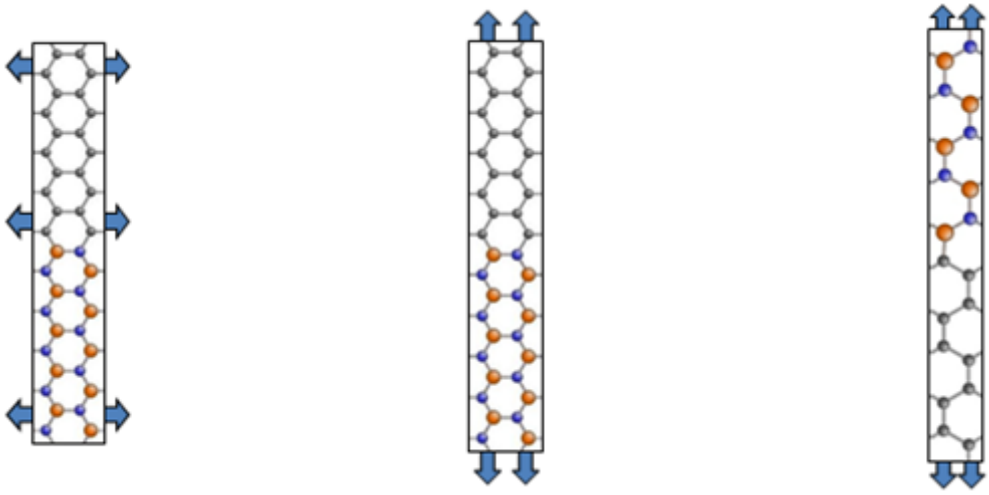

(a) (b) (c)

Fig. 3.9 Parallel (a) and perpendicular (b) direction of strain on aC-BNSL model and perpendicular direction of strain on zC-BNSL (c).

It is not clear if the Poisson ratio for C-BNSL monolayers is constant or not. Hence we need to find every Poisson ratio with respect to different strains. The width of models in this research covers from 14.60 Å to 59.44 Å for aC-BNSL and 21.57 Å to 47.45 Å for zC-BNSL models. I chose two intermediate sized models as example models, one from aC-BNSL and one from zC-BNSL, to calculate the Poisson ratio for these models with respect to all the strains.

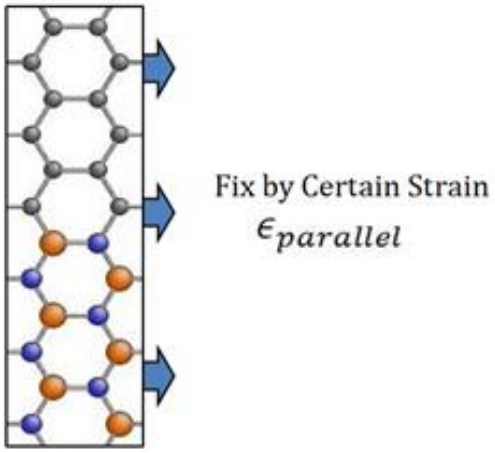

Fig. 3.10 Applying the fixed strain of the specific direction on the example model.

One route to find the Poisson ratio is to fix the strain on the specific direction, then vary the strain in the perpendiculat direction. Following this approach, we consider following procedures to get the Poisson ratio for a fixed strain in a specific direction of a particular model. Firstly, we apply this fixed strain, e.g. $\epsilon_{parallel}$, on the example C-BNSL model in that specific direction as shown in Fig.3.10. Then, we vary the other direction by several very small incremental strains as shown in Fig. 3.9. We calculated the total energy for each incremental strain. By collecting all the data, there will be a smooth curve of total energy with respect to different incremental strains. It will have a C-BNSL model whose total energy is a minimum. The two strains from this model, fixed strain $\epsilon_{Parallel}$ and the varying strain $\epsilon_{Perpendicular}$, can be used to calculate the Poisson

ratio by its definition $\nu = -\epsilon_{Perpendicular}/\epsilon_{Parallel}$. Finally, this is the Poisson ratio for the certain strain, $\epsilon_{parallel}$, on the example C-BNSL model in that specific direction.

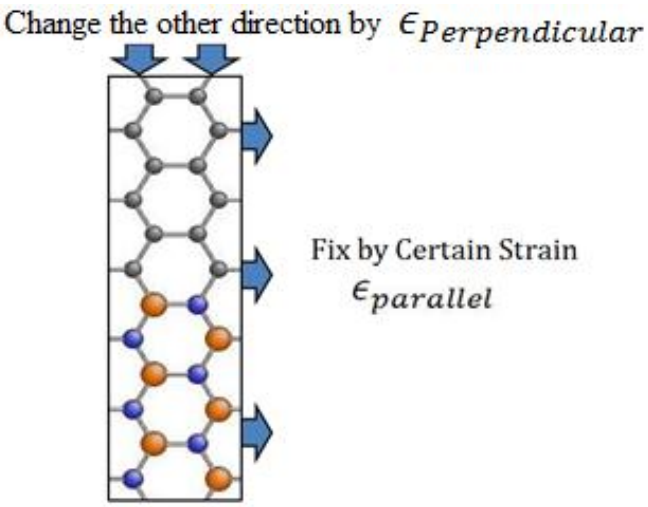

Fig. 3.11 Changing the other direction due to large deformation Poisson effect.

We used 5 % parallel strain on aC-BNSL24 model. The incremental strain varied from -0.003 and up to -0.0145. After the calculation of total energy, the energy curve with respect to incremental strain is illustrated in Fig. 3.12.

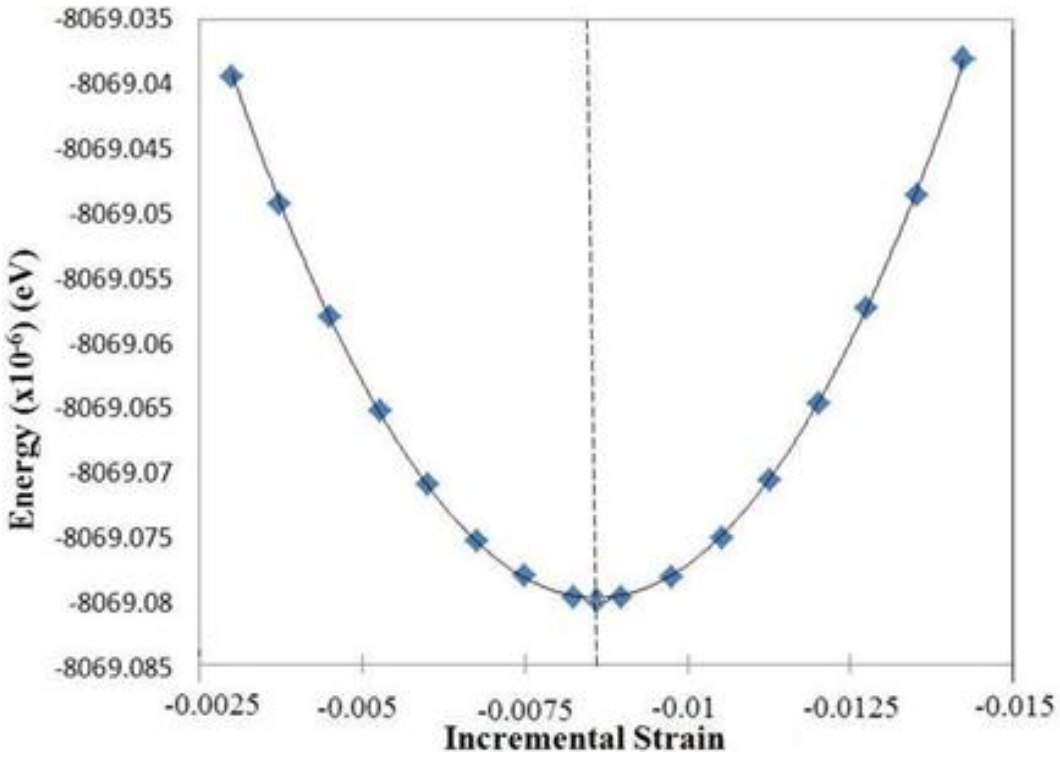

Fig. 3.12 Energy curve for 5 % parallel strain on aC-BNSL24 model via incremental strain. Dash line indicates the corresponding incremental strain.

The dash line in Fig. 3.12 indicates the minimum energy configuration. Two strains from this model can be used to calculate the Poisson ratio for 5 % parallel strain on aC-BNSL24 model. Since the incremental strain from that model is -0.00859, the Poisson ratio is calculated as $\nu = -\epsilon_{Perpendicular}/\epsilon_{Parallel} = -(-0.00859)/0.05 = 0.1718$. Therefore, the Poisson ratio for 5 % parallel strain on aC-BNSL24 model is 0.1718. For the other strain cases, Poisson ratios can be found by the same steps. Fig 3.13 shows Poisson ratio changes when parallel strains increases from 1 % to 20 % on aC-BNSL24 models. The same procedure can be applied to find out the Poisson ratios for corresponding perpendicular strain of aC-BNSL24 (Fig. 3.14). Since the Poisson ratio for 1 % perpendicular strain is over 0.5, therefore the 1 % perpendicular strain will not be applied for the electronic band structure calculation.

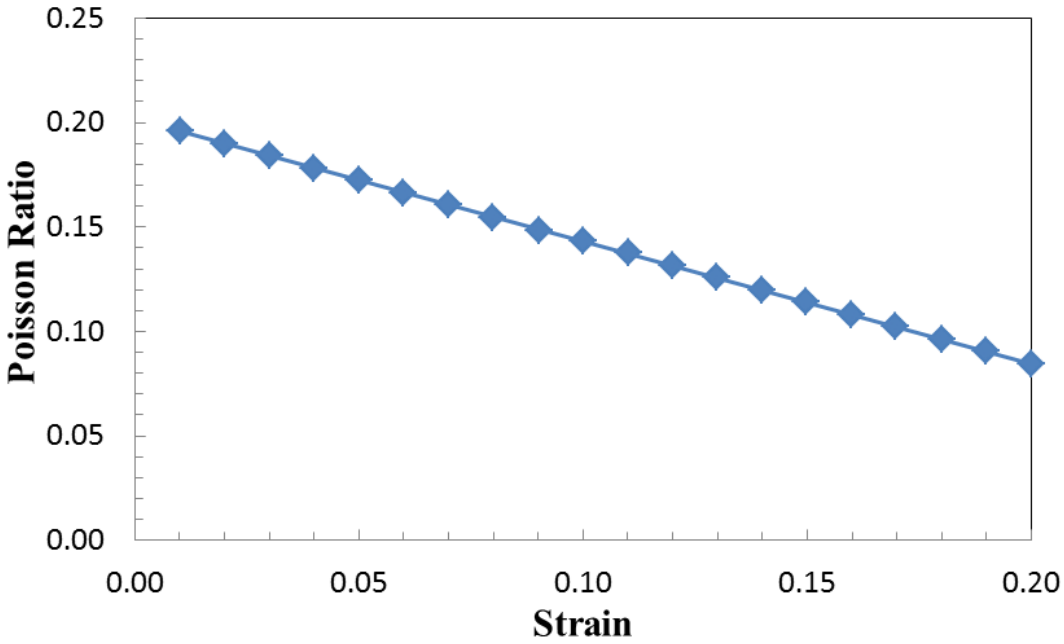

Fig. 3.13 Poisson ratios for parallel strain for aC-BNSL24.

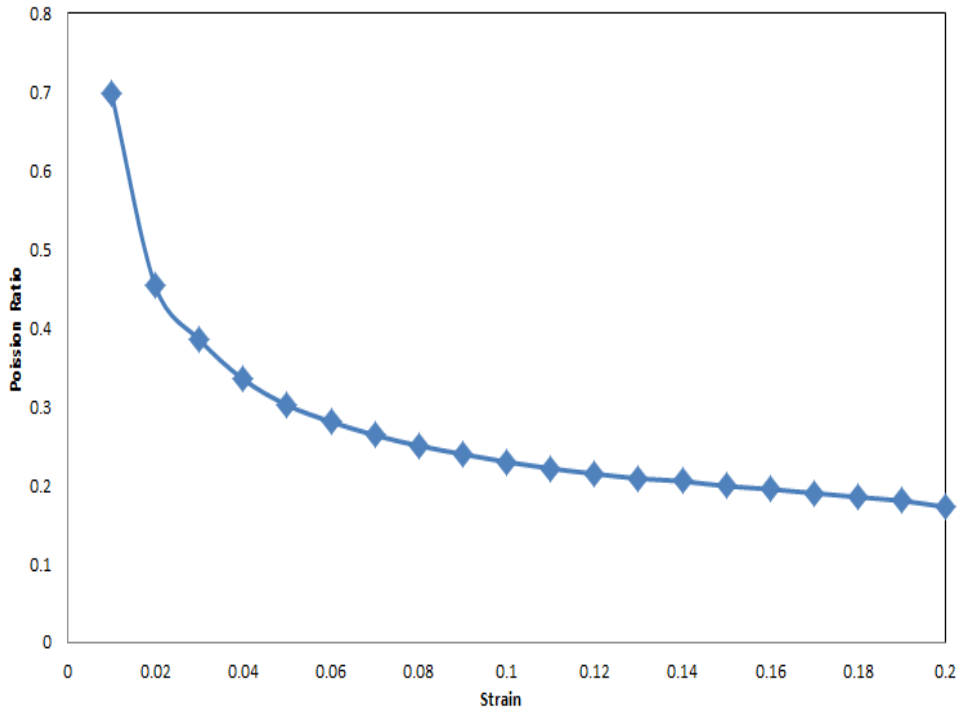

Fig. 3.14 Poisson ratios for perpendicular strain for aC-BNSL24.

We applied the similar procedure to zC-BNSL models to find the Poisson ratio for perpendicular strain. Fig. 3.15 illustrates all the Poisson ratios from the two example models.

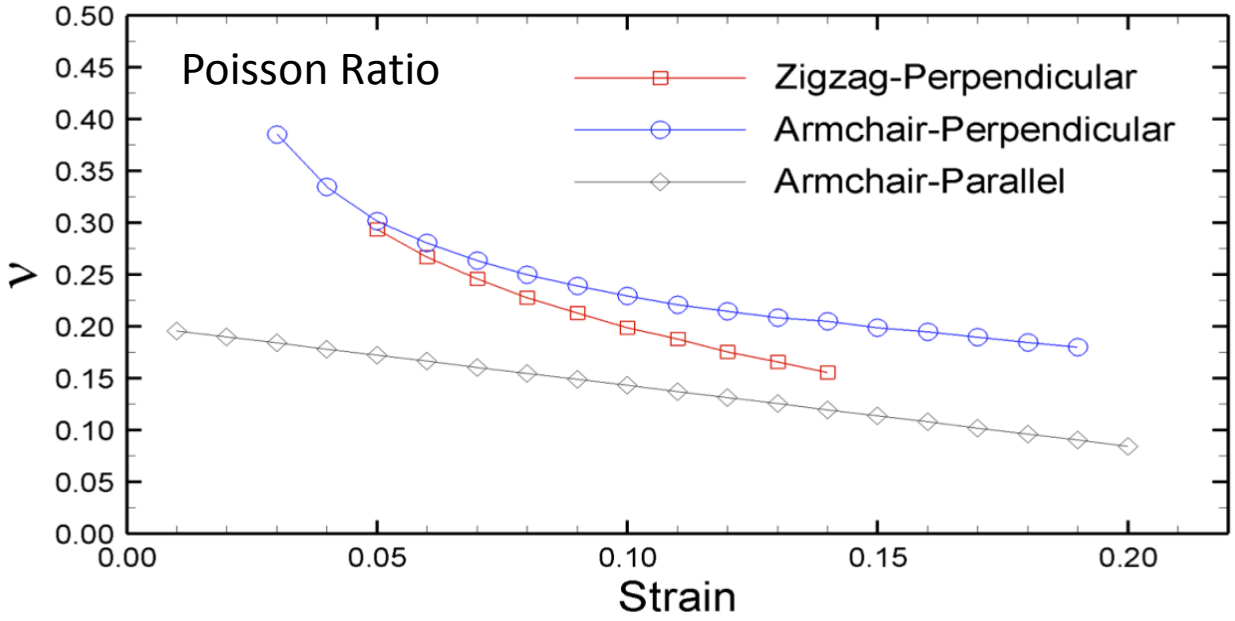

Fig. 3.15 Poisson ratios for different models and different direction of strain.

All the Poisson ratios from Fig. 3.15 are from the two example models, aC-BNSL24 and zC-BNSL16. To compare the Poisson ratio for same strain on different models, we tested a specific value of strain, 15 % of strain for aC-BNSL and 10 % of strain for zC-BNSL. We calculated the Poisson ratio with respect to 15 % parallel strain on several other aC-BNSL models, aC-BNSL08, aC-BNSL16, aC-BNSL32 and aC-BNSL40. All the Poisson ratios from these above models and also the example model are listed in table 3.2.

Table 3.2 Poisson ratios with respect to 15 % parallel strain on different aC-BNSL models.

Different aC-BNSL Models	Poisson Ratio (15 % Parallel Strain)
aC-BNSL08	0.111091756
aC-BNSL16	0.113413817
aC-BNSL24	0.115218773
aC-BNSL32	0.116456094
aC-BNSL40	0.117185623

From table 3.2, the difference between the Poisson ratio from the example model and the ones from the other aC-BNSL models is quite small. The difference is within 0.5 %. It is negligible for the numerical calculations. Thus, the Poisson ratio from the example models can be used on all the other models for the parallel strain. We calculated the Poisson ratio for the 15 % perpendicular strain on other aC-BNSL models and 10 % perpendicular strain on other zC-BNSL models and compared the results to the Poisson ratios from the example models. The data is shown in table 3.3 and 3.4.

Table 3.3 Poisson ratios with respect to 15 % perpendicular strain on different aC-BNSL models.

Different aC-BNSL Models	Poisson Ratio (15 % Perpendicular Strain)
aC-BNSL08	0.196833596
aC-BNSL16	0.197636776
aC-BNSL24	0.198971049
aC-BNSL32	0.199257623
aC-BNSL40	0.201358236

Table 3.4 Poisson ratios with respect to 10 % perpendicular strain on different zC-BNSL models.

Different zC-BNSL Models	Poisson Ratio (10 % Perpendicular Strain)
zC-BNSL10	0.201666281
zC-BNSL16	0.202368723
zC-BNSL22	0.203856296

Similar to the result from the comparison of Poisson ratio of 15 % parallel strain on aC-BNSL monolayers, there is no large difference between the Poisson ratio from the example model and the Poisson ratios from all the other different C-BNSL models. This is a small difference for

numerical calculation. Therefore, we used the Poisson ratios from the example models on all the other C-BNSL monolayers.

After the strain and the corresponding Poisson ratio are applied on the C-BNSL models, another minimization is needed. This minimization is a test whether the atomic position changes. The results indicates that the atomic position do not change after the minimization. Therefore, the Poisson ratio from our calculations can properly reflect the length compressed on the direction perpendicular to the strain direction.

Chapter 4

Numerical Results and Discussions

4.1 Armchair C-BNSL Models subject to Strain

After we developed a method to build the C-BNSL models, and computed the Poisson ratios with respect to strains on different directions, we formed the strained C-BN superlattice models and considered the large deformation Poisson effect. The first-principles calculation, which is based on the density functional theory, was used to calculate their band structures and get their energy gaps.

Since there are different strain cases and models with different width in this study, we considered the following steps to compute the band structure calculations for aC-BNSL models with strains. Take parallel strain on aC-BNSL models as an example. First, we chose a specific aC-BNSL model, say aC-BNSL24, and applied all the strains and their matching Poisson ratio on this model. We calculated the band structure and got the energy gap for each strain case**,** and collected the data. An energy gap curve for aC-BNSL24 was developed with respect to all the strain, as Fig. 4.1 shown. After this, we applied the same procedure for the other aC-BNSL models. Therefore, we have several energy gap curves for each specific aC-BNSL model with respect to all the strain on it. Finally, we combined all the energy gap curves together to form a 3D plot of energy gaps of aC-BNSL models with respect to all parallel strain as shown in Fig. 4.2. In this plot, the energy gaps changes not only with respect to the width of the models, but also with respect to strain. In Fig. 4.2, the model width direction is marked as the model number. The model number is set as the number of conventional unit cell in the width direction. It means

the width of a model equals to the number of conventional unit cells in the width direction times lattice constants in width direction.

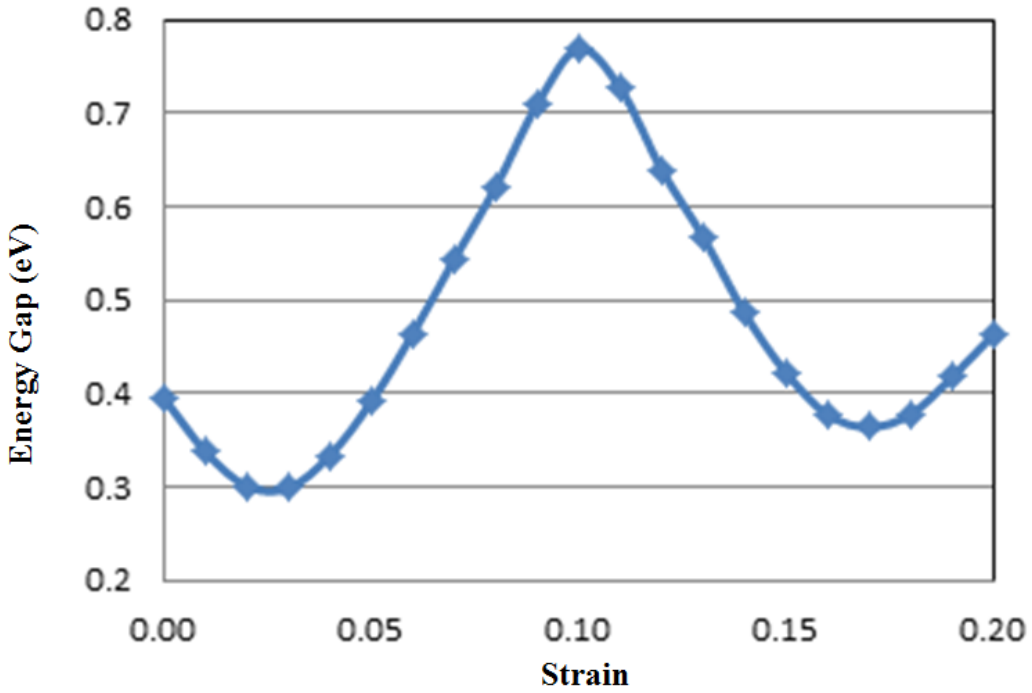

Fig. 4.1 Energy gap curve for aC-BNSL24 with parallel strain.

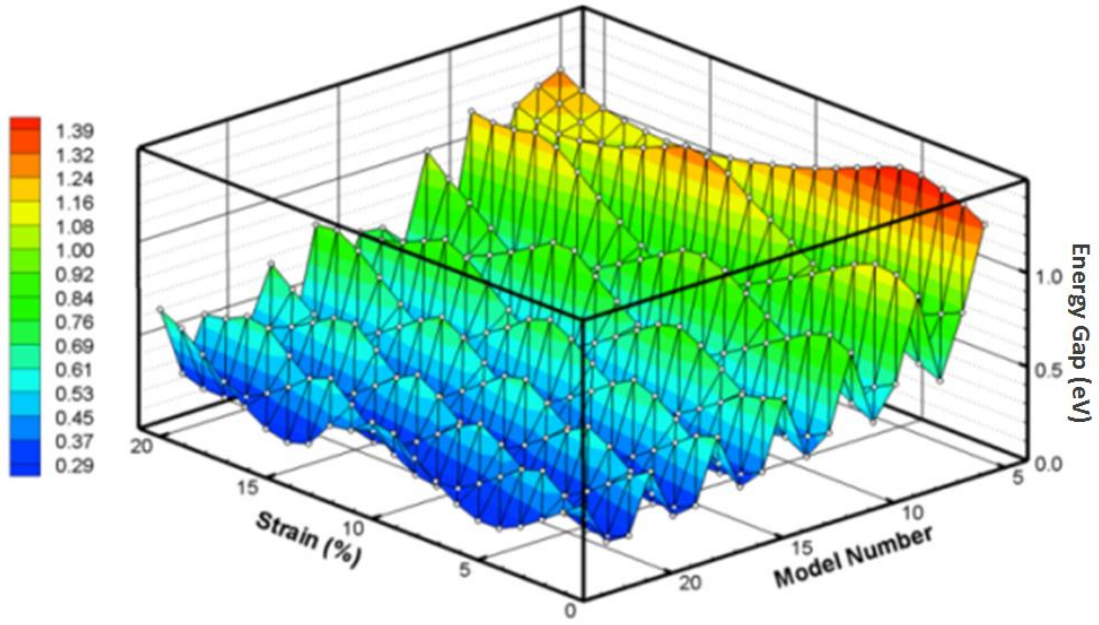

Fig. 4.2 3D plot of energy gap of aC-BNSL subject to parallel strain.

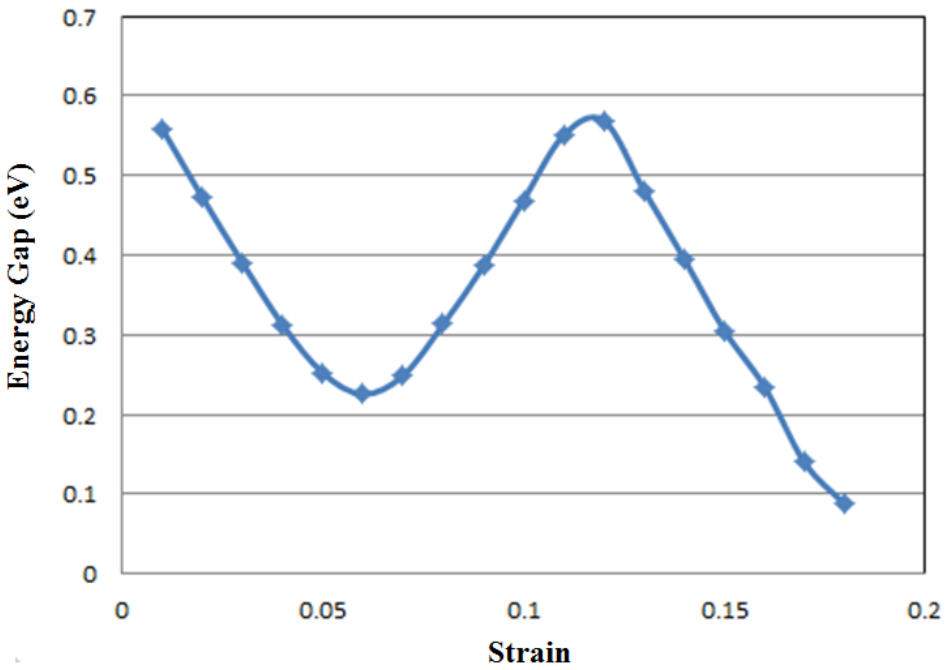

Fig. 4.3 Energy gap curve for aC-BNSL24 with perpendicular strain.

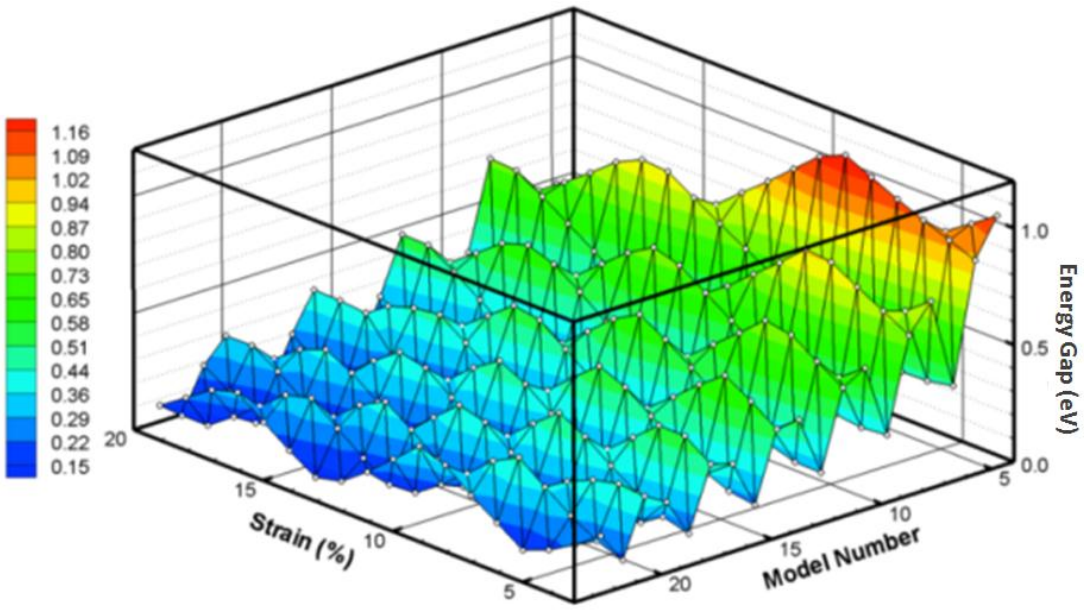

Fig. 4.4 3D plot of energy gap of aC-BNSL subject to perpendicular strain.

The same steps were applied to calculate energy gaps for aC-BNSL model with respect to perpendicular strains. Firstly, we can get an energy gap curve for a specific model (Fig. 4.3). A

similar 3D energy gap plot with respect to strain value and model width is shown in Fig. 4.4. And the model width is also marked as the model number as same as what we did in the energy gap plot for parallel strain. Fig. 4.2 and 4.4 indicate that the band gaps for strained aC-BNSL models oscillate not only with respect to the strain, but also with respect to the width of the models.

To see the results more clearly, we plotted results on a contour. One plot contour is shown in Fig 4.5. In the contour plot, the red area indicates a larger energy gap and the blue area represents a smaller energy gap. From the Fig. 4.5 we can tell, no matter what the direction of strain is applied on the aC-BNSL models, the pattern of the energy gap is very similar. The pattern always goes to the diagonal direction of the combination of strain direction and the width direction.

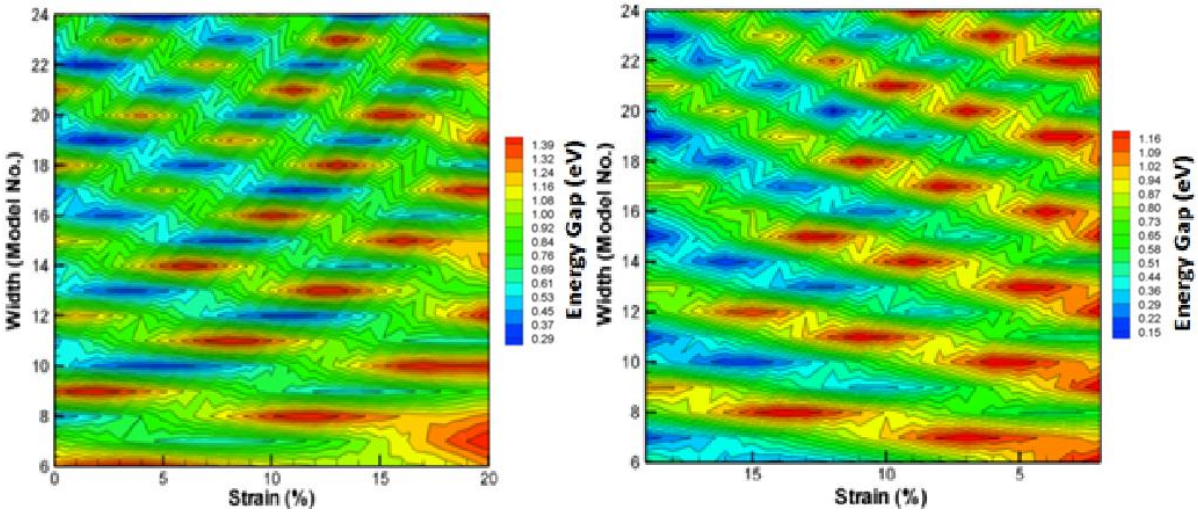

(a) (b)

Fig.4.5 Contour plot of aC-BNSL with parallel strain (a) and perpendicular strain (b)

The other 2-D plot is a lateral view from the strain axis which is shown in Fig 4.6. In the lateral view of the energy gap, each vertical line represents the range of the energy gap for the model

with specific width. The point at the top for each vertical line represents the largest energy gap for this specific model. The point at the bottom for each vertical line represents the smallest energy gap. For both parallel and perpendicular strain cases, largest and smallest energy gap values are both decreasing with respect to increasing aC-BNSL model width (Fig. 4.6). However, there are no zero energy gaps, which means that physically there is no band gap close for aC-BNSL models when we apply strain on them. Fig. 4.6 indicates that there is no energy gap larger than 2 eV for strained aC-BNSL models.

The electronic properties of metal, semiconductor and insulator can be indicated by the band gaps. The electronic band structure of metals shows an overlap of the valence band and the conduction band, which means the band gap is zero. The electronic band structure of insulators has separation between the valence band and the conduction band with a relatively large band gap (>2 eV). The electronic band structure found in the semiconductors is the same as for insulators except that the band gap is relatively narrow (<2 eV).

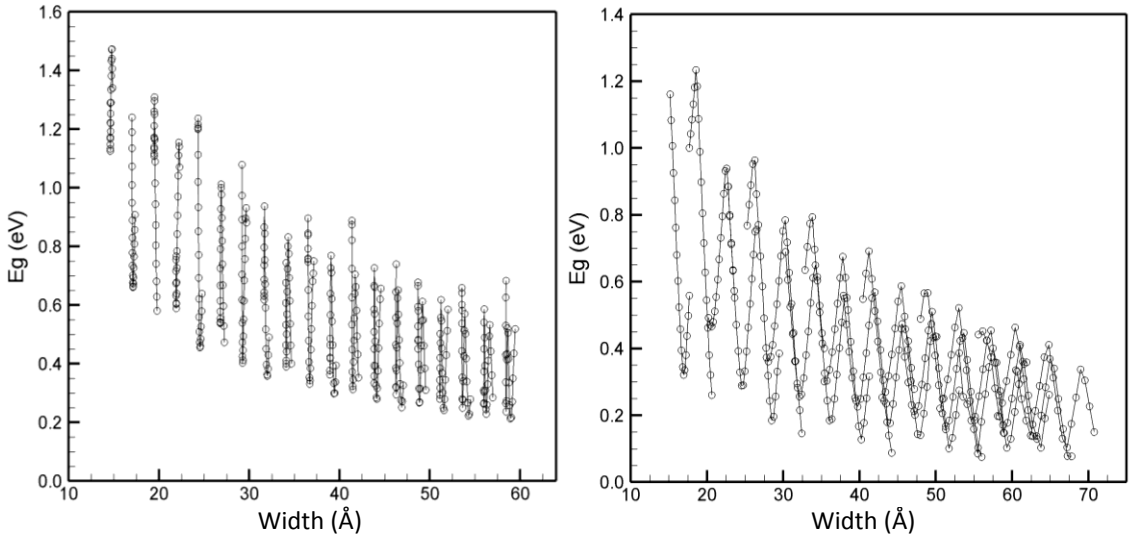

(a) (b)

Fig.4.6 Lateral view plot of aC-BNSL with parallel strain (a) and perpendicular strain (b)

Since band gaps for strained aC-BNSL models are in the range which is larger than 0 eV and smaller than 2 eV, therefore there is no change of electronic state when we apply parallel or perpendicular strains and their corresponding Poisson ratio on aC-BNSL models.

4.2 Zigzag C-BNSL Models subject to Strain

For zigzag C-BN superlattice models, we apply the spin-polarized calculation. The spin-polarized edge states are obtained in the calculations that correspond to antiferromagnetic (AF) alignments of the spin moments at opposite edges of the zC-BNSL models. In the SIESTA program, the spin directions of electrons of two carbon atoms on the C-BN boundary were given by the opposite directions. One is the α spin, which is in the spin-up direction. Other is the β spin, which is the spin-down direction. In the electronic band structures of strained zC-BNSL models, the red line represents the band structure of the spin-up electron and the blue line represents the band structure of the spin-down electron. The overlap of the band structures of the spin-up and spin-down electrons near the Fermi level indicates the same electronic properties they have. The separation of the two electrons represents that these two electrons have different electronic properties.

Before we apply strain on the zC-BNSL models, we calculated band structure for several zigzag C-BNSL models without applying strain. Fig. 4.7 illustrates the electronic band structure of some zC-BNSL models without strain. It shows separation of band structure between spin-up electron and spin-down electron in some of the zC-BNSL models.

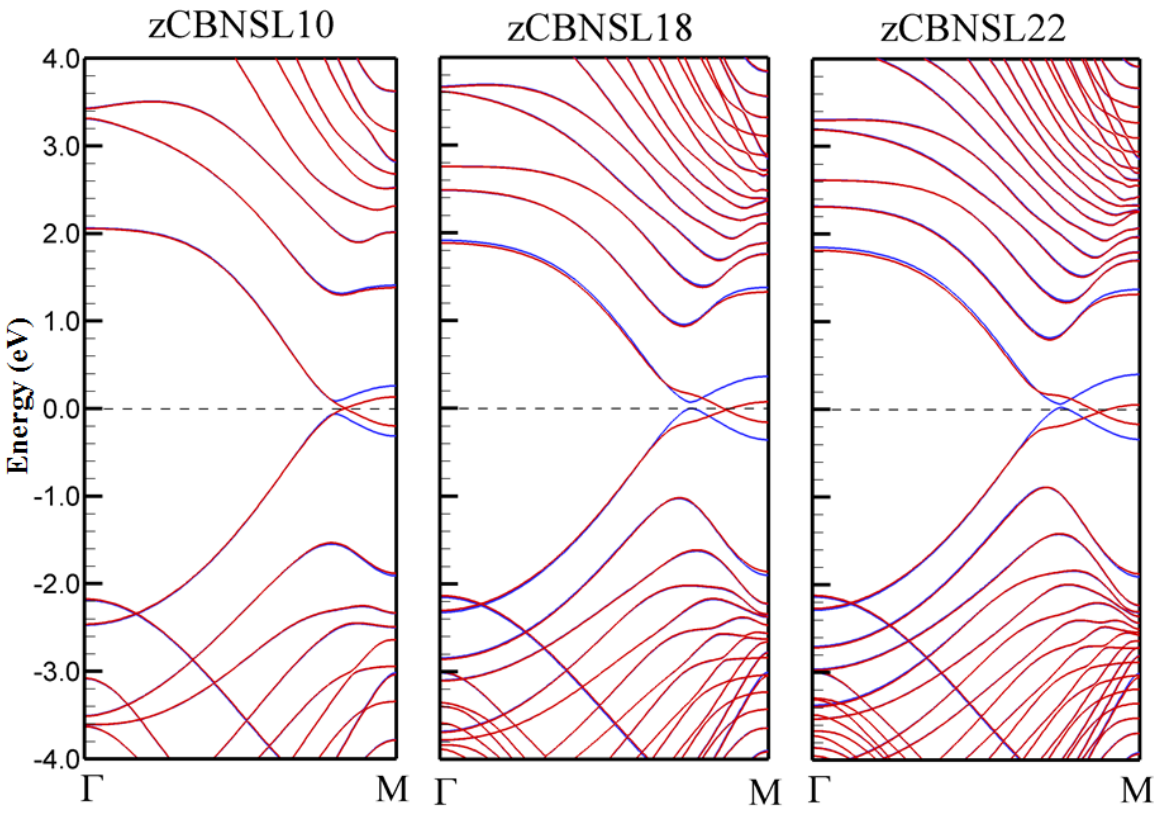

Fig. 4.7 Electronic Band structure for different zC-BNSL models without strain.

We calculated the electronic band structure for all the zigzag C-BN superalttice models without applying strain. The results are shown as Fig. 4.8. We found that the energy gap for spin-up and spin-down curves overlap and are both not zero for small zC-BNSL models. This status, spin-up and spin-down electrons both with a same open energy gap, means the electronic property of the semiconductor. Then the separation appears when we increase the width of zC-BNSL models. It has an open energy gap for spin-down electron and a close energy gap for spin-up electron. This period gives us an electronic property of half-metallic. Finally, when the width keeps increasing, we can find that the spin-up and spin-down electrons overlap again and both have the close energy gap. This status gives us an electronic property of metal. The whole procedure of increased width of zC-BNSL models provides us a transition of electronic property of zC-BNSL from the semiconductor to half-metallic, and finally to metal.

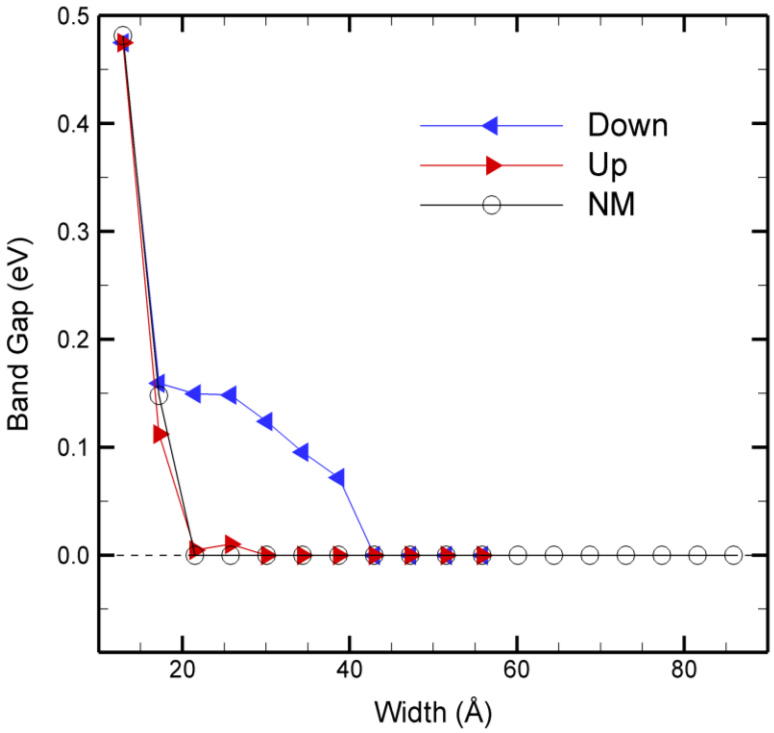

Fig. 4.8 Spin polarized zC-BNSL energy gaps without strain.

Next, strains were applied on the zC-BNSL models to see if the mechanical strain and the Poisson effect of large deformation will change the electronic property of the zC-BNSL models. The direction of strain we will apply on the zC-BNSL models is the perpendicular strain as mentioned above in Section 3.4, which is illustrated in the Fig. 4.9. The procedure to calculate the electronic band structure of zC-BNSL models with strain is similar to the steps in Section 4.1 for the band structure calculation of strained aC-BNSL models. We will choose a zC-BNSL model, apply all the strains and their corresponding Poisson ratio on this model, and finally calculate the electronic band structure.

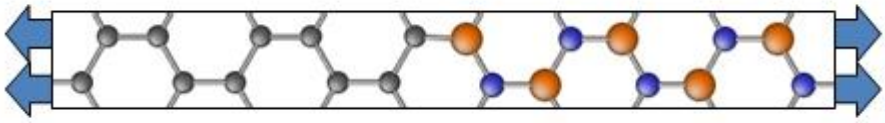

Fig. 4.9 The direction of perpendicular strain on zC-BNSL10.

First, we calculated band structure of a small zC-BNSL model, zC-BNSL10. The electronic band structure of zC-BNSL10 with increasing strain is illustrated in Fig. 4.10. From Fig. 4.10, we found that there is still the separation between spin-up curve and spin-down curve when we increased strain up to 6 % and 10 %. Furthermore, when the strain is up to 13 %, the spin-up electron shows an open energy gap which was initially closed. This process of opening a band gap can provide us a transition of electronic properties from semi-metallic to semiconductor which means the strain on zC-BNSL10 models can tune its electronic properties.

Next, we calculated electronic band structure for a large zC-BNSL model, zC-BNSL 20. The result is shown as Fig. 4.11. With respect to the increasing strain, a separation between spin-up and spin-down at 7 % strain, and shows the band gap open for spin-up band at 11 % strain. More surprisingly, we found that at 13 % strain, there shows a close band gap for spin-down which was initially open.

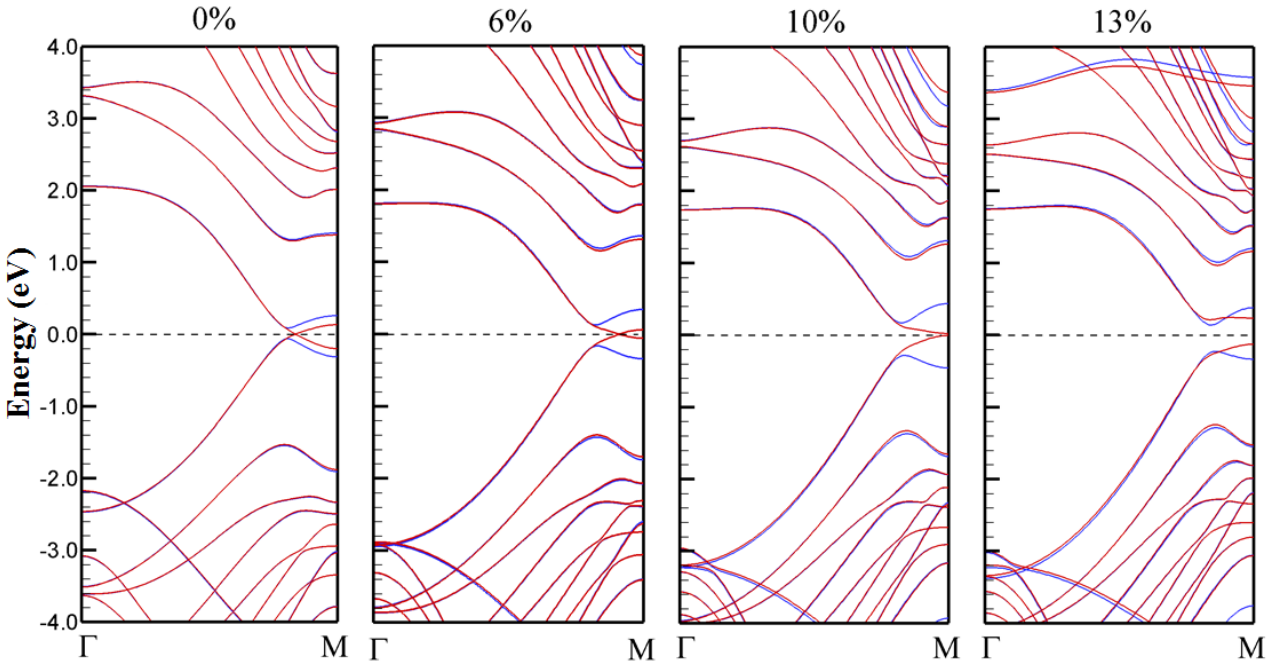

Fig. 4.10 Electronic band structures of zC-BNSL10 with increasing perpendicular strain

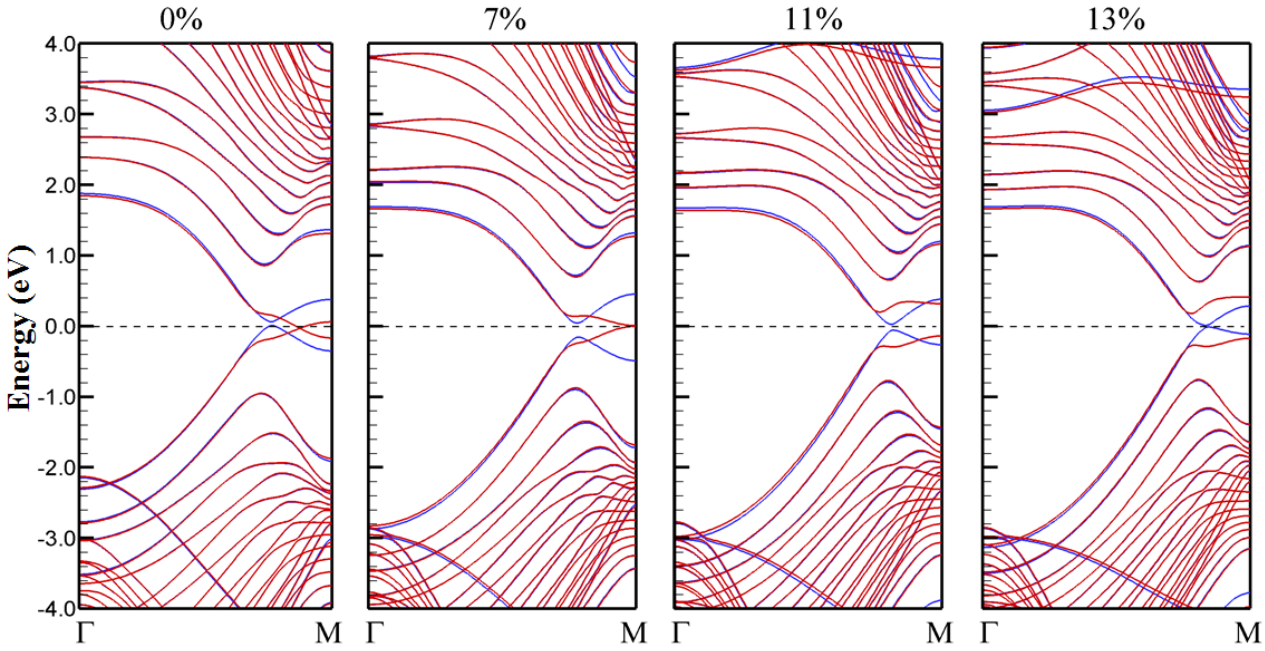

Fig. 4.11 Electronic band structures of zC-BNSL20 with increasing perpendicular strain.

The pattern of electronic band structure for zC-BNSL20 with respect to increasing perpendicular strain is showing the separation of spin-up band and spin-down band and the opening for spin-up band and the closing for spin-down band. This pattern can tailor the electronic properties of zC-BNSL20 from semi-metallic to semiconductor, finally to semi-metallic again.

With this remarkable result, we did the electronic band structure calculation of all the zC-BNSL models with respect to the increasing perpendicular strain. We computed the band gap for both spin-up electron and spin-down electron. The results are shown in Fig. 4.12. We found that all the band gaps of spin-up electron have a similar pattern with respect to the increasing strain, so do the spin-down band gaps. For spin-up electron as shown in Fig. 4.12 (a), initially the energy gap is close, when the strain increases the energy gap begins to open at a certain point of strain. After this point, the energy gaps keep becoming larger quickly with respect to the increasing strain. For large zC-BNSL models, the energy gaps of spin-up electron stop to increase quickly and the band gaps stay between 0.3 eV and 0.4 eV.

For spin-down band gaps as illustrated in Fig. 4.12 (b), initially the energy gap is open, and becomes larger when the strain increases. At some specific point of strain, the energy gap begins to fall and keep falling with respect to the increasing strain.

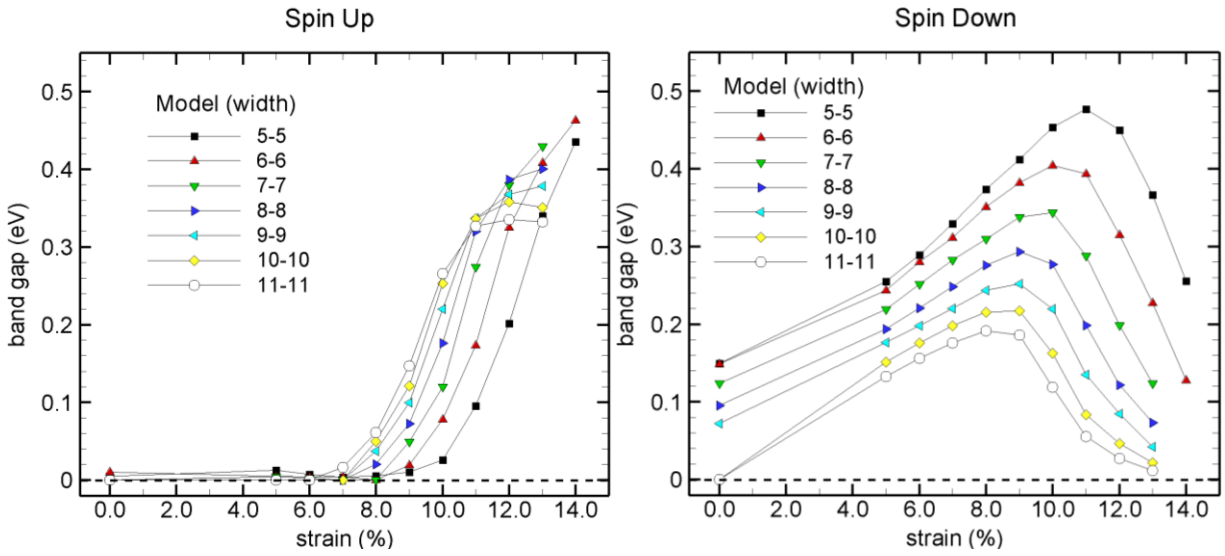

(a) (b)

Fig. 4.12 Changing pattern of spin-up (a) and spin-down (b) band of zC-BNSL subject to perpendicular strain.

Chapter 5

Conclusion

In this research, we have studied how to determine the lattice constant of individual graphene and boron nitride monolayers, the method to build C-BN superlattice model, how to account for a large deformation Poisson effect on C-BNSL monolayer and how to find the Poisson ratio with respect to the corresponding strain. Finally, we calculated the electronic band structure for aC-BNSL and zC-BNSL respectively. In the process, we found that energy gap values for strained aC-BN superlattice monolayers oscillate with respect to not only strain, but also with respect to the model width regardless of direction of strain applied on the aC-BNSL models. The range of energy gap for strained aC-BNSL monolayer is 0.2 -1.5 eV for parallel strain and 0.05 – 1.2 eV for perpendicular strain. Obviously, there is no close energy gap or energy gap over 2 eV for strained aC-BNSL monolayer, which means there is no electronic property changing when we apply strain on aC-BNSL monolayer. For zigzag C-BNSL monolayer, we did the spin-polarized calculation. We added spin direction for the specific two carbon atoms in the zC-BNSL supercells. The two carbon atoms are at the zigzag C-BN boundary and we define these carbon atoms with opposite spin directions. After the electronic band structure calculation, we found that strain can change the spin properties of zigzag C-BNSL monolayer. Furthermore, strain can not only open a band gap for spin-up band, but also can close a band gap for spin-down band of zC-BNSL monolayer. This process can bring a transition of zC-BNSL monolayer from metal to half-metallic, and then to a semi-conductor. It means the mechanical strain on zC-BNSL monolayer can change its electronic property. This finding has significant meaning, since the electronic property can be changed only by applying strain and considering large deformation

Poisson effect. This unusual electronic property of C-BN superlattice monolayer makes it a promising nanomaterial for building electronic devices. For future research, we will continue to investigate the heterostructures which is based on graphene and boron nitride monolayer.

References

[1] D. Akinwande, and H. S. P. Wong, Carbon Nanotube and Graphene Device Physics. Cambridge University Press. pp. 47–49 (2011).

[2] K. S. Novoselov, A. K. Geim, S. V. Morozov, D. Jiang, Y. Zhang, S. V. Dubonos, I. V. Grigorieva, and A. A. Firsov, Science. **306**, 666, (2004).

[3] C. Lee, *et al.*, Science. 321 (5887): 385-8, (2008).

[4] C. Jin, F. Lin, K. Suenaga, and S. Iijima, Phys. Rev. Lett. **102**, 195505 (2009).

[5] J.C.Meyer, A. Chuvilin, G. Algara-Siller, J. Biskupek, and U. Kaiser, Nano Lett. **9**, 2683 (2009).

[6] R. Heyrovska, arXiv: **0804.4086** [physics.gen-ph](2009).

[7] B. Huang, H. Lee, B.L. Gu, F. Liu, and W. Duan, arXiv:**1011.6010v1** [cond-mat.mes-hall] (2010).

[8] L. Ci *et al.*, Nature Material. DOI: **10.1038/NMAT2711** (2010).

[9] F. Liu, P. Ming, and J. Li, Phys. Rev. B **76**, 064120 (2007).

[10] F. M. D. Pellegrino, G. G. N. Angilella, and R. Pucci, Phys. Rev. B **81**, 035411 (2010).

[11] R. Heyd, A. Charlier, and E. McRae, Phys. Rev. B **55**, 6820 (1997).

[12] L. Yang, M. P. Anantram, J. Han, and J. P. Lu, Phys. Rev. B **60**, 13874 (1999).

[13] T. W. Tombler *et al.*, Nature (London) **405**, 769 (2000).

[14] L. Yang, and J. Han, Phys. Rev. Lett. **85**, 154 (2000).

[15] E. D. Minot, Y. Yaish, V. Sazonova, J. Y. Park, M. Brink, and P. L. McEuen, Phys. Rev. Lett. **90**, 156401 (2003).

[16] M. L. Teague *et al.*, Nano Lett. **9**, 2542 (2009).

[17] N. Ferralis, R. Maboudian, and C. Carraro, Phys. Rev. Lett., **101**, 156801 (2008).

[18] G. Gui, J. Li, and J. Zhong, Phys. Rev. B, **78**, 075435 (2008).

[19] M. Mohr, K. Papagelis, J. Maultzsch, and C. Thomsen, Phys. Rev. B, **80**, 205410 (2009).

[20] S. M. Choi, S. H. Jhi, and Y. W. Son, Phys. Rev. B, **81**, 081407 (2010).

[21] Z. H. Ni *et al.*, ACS Nano, **2**, 2301-2305 (2008)

[22] F. Guinea *et al.*, Nat. Phys., **6**, 30-33 (2010)

[23] Y. B. Zhang *et al.*, Nature, **459**, 820-923 (2009)

[24] R. Balog *et al.*, Nat. Mater, **9**, 315-319 (2010)

[25] J. O. Sofo *et al.*, Phys. Rev. B, **75**, 153401 (2007)

[26] Y. F. Li *et al.*, J. Phys. Chem. C, **113**, 15043-15045 (2009)

[27] H. J. Xiang *et al.*, Nano Lett., **9**, 4025-4030 (2009)

[28] L. M. Xie *et al.*, J. Am. Chem. Soc., **132,** 14751-14753 (2010)

[29] L. C. Campos *et al.*, Nano Lett., **9**, 2600-2604 (2009)

[30] D. V. Kosynkin *et al.*, Nature, **458**, 872-876 (2009)

[31] M. Terrones, Nature, **458**, 845-846 (2009)

[32] L. Jiao *et al.*, Nature, 458, 877-880 (2009)

[33] X. R. Wang *et al.*, Nat. Chem., 2, 661-555 (2010)

[34] J. Li, and V. B. Shenoy, arXiv:**1009.5658v1** [cond-mat.mes-hall] (2010).

[35] S. S. Yu, W. T. Zheng, Q. B. Wen, and Q. Jiang, Carbon. **46**, pp. 537-543 (2008).

[36] C. H. Park and S. G. Louie, Nano Lett. **8**, 2200 (2008).

[37] S. Jun *et al.*, Phys. Rev. B, **83**, 153407 (2011).

[38] W. Q. Han, Y. Bando, K. Kurashima, and T. Sato, Chem. Phys. Lett. **299**, 368 (1999) .

[39] L. S. Panchakarla, A. Govindaraj, and C. N. R. Rao, ACS Nano **1**, 494 (2007) .

[40] R. Czerw, M. Terrones, J. C. Charlier, X. Blase, B. Foley, R. Kamalakaran, N. Grobert, H. Terrones, D. Tekleab, P. M. Ajayan, W. Blau, M. Rühle, and D. L. Carroll, Nano Lett. **1**, 457 (2001).

[41] J. Liu, S. Webster, and D. L. Carroll, Appl. Phys. Lett. **88**, 213119 (2006).

[42] A. J. Du, S. C. Smith, and G. Q. Lu, Chemical Physics Lett. **447** 181-186 (2007).

[43] P. Honhenberg and W. Kohn, Phys. Rev. **136**, B864 (1964).

[44] W. Kohn and L. J. Sham. Phys. Rev. **140**, A1133 (1965).

[45] David S.Sholl Janice A. Steckel, Density Functional Theory: A Practical Introduction, pp7-14, John Wiley & Sons. Inc.

[46] R. C. Cammarata, Prog. Surf. Sci. **46**, 1 (1994).

[47] J. Soler. E. Artacho, J. D. Gale, A. Garcia, J. Junquera, P. Ordejon, and D. Sanchez-Portal, J. Phys.: Condens. Matter **14**. 2745 (2002).